Circuit Mechanisms Underlying Chromatic Encoding in *Drosophila* Photoreceptors

Sarah L. Heath

Submitted in partial fulfillment of the
requirements for the degree of
Doctor of Philosophy
under the Executive Committee
of the Graduate School of Arts and Sciences

COLUMBIA UNIVERSITY

2021

Abstract

Circuit Mechanisms Underlying Chromatic Encoding in Drosophila Photoreceptors

Sarah L. Heath

Color vision is widespread in the animal kingdom, and describes the ability to discriminate between objects purely based on the wavelengths that they reflect. Experiments across many species have isolated wavelength comparison in the brain as a computation underlying color vision. This comparison takes place in color opponent neurons, which respond with opposite polarity to wavelengths in different parts of the spectrum. In this work, I explore color opponency in the genetically tractable organism *Drosophila melanogaster*, where these circuits have only just begun to be described. Using two-photon calcium imaging, I measure the spectral tuning of photoreceptors in the fruit fly and identify circuit mechanisms that give rise to opponency. I find two pathways: an insect-specific pathway that compares wavelengths at each point in space, and a horizontal-cell-mediated pathway similar to that found in mammals. The horizontal-cell-mediated pathway enables additional spectral comparisons through lateral inhibition, expanding the range of chromatic encoding in the fly. Together, these two pathways enable efficient decorrelation and dimensionality reduction of photoreceptor signals while retaining maximal chromatic

information. This dual mechanism combines motifs of both an insect-specific visual circuit and an evolutionarily convergent circuit architecture, endowing flies with the ability to extract chromatic information at distinct spatial resolutions.

Table of Contents

List of Charts, Graphs, Illustrations

Acknowledgments

One thing this journey has taught me about being a scientist- you *always* end up realizing, in one way or another, that the world never works how you expected it to. The road through the scientific method is in fact long and winding, and there is no way I could have made it out the other side alone.

In terms of my growth as a scientist, there are so many people I would like to thank. Firstly, I would like to thank my mentor, Rudy. We started on this journey into the unknown with Jessie, and together built a lab family that inspires and supports each other. We faced many roadblocks on our path to showing the world our discoveries, but somehow, you were always able to convince me that they were just speedbumps. Jessie, words can't describe how valuable your friendship has been to me over the years, both inside and outside of the lab. Gucky, our close working relationship exposed me to things I would have never would have looked for on my own. Thank you for helping me grow and think outside of the box. To my thesis committee and everyone else in the Behnia Lab- I couldn't be more thankful for such a supportive group.

To family and friends in my personal life that have been there for all the ups and downs- you know who you are. I love you all very much. Lastly, to my #1 – I wouldn't be here without you. I will always love you for pushing me to find my passion, but also my peace.

Chapter 1: Introduction

The visual landscape that exists in the world is comprised of a complex combination of colors and patterns, which ultimately need to be processed by the brain to extract meaningful information. Thus, color vision is a crucial tenet of visual processing, and is widespread in the animal kingdom [1]. It has been shown to inform a myriad of vital behaviors such as seeking food, mating, navigating, and identifying predators [1]. Extensive work in primates has shed much light on the mechanisms of detecting chromatic information at the retinal level, and also the basics of color perception on a behavioral level [2]. However, the circuit mechanisms that transform stimulus information into color percepts remain largely unexplained. Looking forward, studies exploring the neuronal and behavioral outputs of color circuits in more "simple" model organisms can help us to determine if brains of vastly different sizes show convergence in solutions to spectral processing problems.

1.1 The Spectral Sensitivity of Photoreceptors

At its core, color vision is the ability to perceive differences in wavelengths of light, regardless of variations in intensity. This necessitates that an animal must possess photoreceptors with different spectral sensitivities, as a single photoreceptor type cannot distinguish between changes in wavelength or intensity

[3]. The spectral sensitivity of a photoreceptor describes its probability to absorb a photon of a given wavelength, which is then converted to a neural signal via the phototransduction pathway, where the identity of the photon is lost [3, 4]. This sensitivity depends on both the specific opsin expressed by photoreceptors, and also on additional filters that exist in the light path such as screening pigments or external lenses. Importantly, different amino acid configurations determine the peak sensitivities of the opsins, which can vary from 300 to 580 nm [5].

Most mammals possess two photoreceptor types, making them dichromatic. However, humans possess three cone types: short (S, ~430 nm), medium (M, ~530 nm) and long (L, ~560), rendering them trichromatic [6]. Trichromatic color vision is considered to be well-suited for encoding the large majority of chromatic content in most visual scenes [7], yet vertebrates such as fish, reptiles, and birds are largely tetrachromatic, endowing them with the potential ability to extract additional spectral information from the environment [8]. Regardless of the number of unique photoreceptor types, it remains a prerequisite to color vision that signals from these different receptors must be compared in the brain [2]. For example, even though mantis shrimp possesses twelve photoreceptor types, they are poor at discriminating between colors that humans, as trichromats, see as distinct [9]. This suggests that the output of these photoreceptors is a rapid behavioral program instead of a wavelength comparison by downstream neurons

[10]. The example of the mantis shrimp highlights how important the comparison of photoreceptor outputs is for true color vision.

1.2 Color Opponent Mechanisms

Comparison of the outputs of multiple photoreceptor types is the most basic computational requirement of a color vision system [2]. Work done in vertebrates and invertebrates alike has revealed that color opponent neurons, which respond with opposite polarity to different wavelengths of light, serve as the substrate for the wavelength comparison necessary for wavelength discrimination [11, 12]. Color opponency is possible due to antagonistic inputs from multiple photoreceptors with different spectral sensitivities, and furthermore, lateral interactions between photoreceptors have been shown to confer a spatial dimension to color encoding [13, 14]. As cone photoreceptors are arranged in a 2D lattice, lateral interactions via horizontal cells are essential for establishing these opponent signals in the retina [15-18]. This results in spectrally opponent signals in downstream cells, which compare chromatic information between neighboring points in visual space through center-surround interactions.

Processing of wavelength information in the retina has been well studied in mammals, where multiple color opponent channels have been reported [12]. It has long been known that color opponent signals are found in retinal ganglion

cells (RGCs) [2], but opponency has been found to arise as early as cone terminals [19, 20]. In primates, signals from photoreceptors pass through bipolar cells to two general classes of RGCs, which mediate the two main opponent channels. So-called ‘‘red-green’’ neurons compare the activity of M and L photoreceptors, and ‘‘blue-yellow’’ neurons compare the activity of S and L+ M photoreceptors (reviewed in [2]). These neurons were originally thought to be yoked to the psychophysical finding of the four perceptual hues (red, blue, green, and yellow), but this has since turned out to be inaccurate [21-23]. Thus, the neural basis for the perception of unique hues most likely involves further processing of opponent signals.

Interestingly, the two axes of opponency encoded at the level of RGCs— red-green and blue-yellow— have been shown to correspond to an optimal decomposition of S, M, and L cone sensitivities [24]. This allows the retina to remove the correlations introduced by the high degree of overlap between cone sensitivities and more efficiently transmit spectral information to downstream visual circuits.

1.3 Color Representation in Higher Brain Areas

Broadly, the two color channels represented in the retina project to anatomically defined regions downstream. “Red-green” RGCs, or midget cells, project to the parvocellular layer of the lateral geniculate nucleus (LGN) [25].

The LGN is a thalamic nucleus that is known to route signals from the retina to the visual cortex. At the level of the LGN, center-surround "red-green" opponent signals continue to be robustly encoded [2]. On the other hand, "blue-yellow" ganglion cells, or small bistratified ganglion cells, project to the koniocellular layers of the LGN [26]. This is, of course, a vast oversimplification, as there are ~20 types of ganglion cells in the retina- the majority of which have not been well-characterized [2]. Thus, while studies in the primate retina and LGN have been extensive, our understanding of is far from complete.

Due to the complexity of the primate brain, much also remains unknown about chromatic encoding higher in the cortex. The primary visual cortex (V1) is the main target of LGN projections. However, how cone signals are transformed in this region remains highly debated. While many V1 neurons are tuned for pattern and orientation, relatively few were found to be specifically tuned to color [27]. While the low quantity of color-selective neurons was surprising, the true controversy arose around the concept of explaining color-form interactions, which are required to explain higher order perceptual phenomena such as color contrast and color constancy. "Double-opponent" cells, or cells where both the center and surround show opponency, are one possible locus to unify both color and form information. However, their existence and properties have been long debated (reviewed in [2]).

In terms of functional organization for color encoding, one simple hierarchical model proposes that color signals propagate from V1 to sub-compartments of V2 called “blobs”, to regions termed “globs” located in V4, and ultimately end up in the inferior temporal cortex (IT) [28-34]. Here, hue-specific neurons have been reported, which have been hypothesized to mediate color perception [31, 35]. However, due to the complexity of the visual cortex in primates, it will likely be many decades before we reach a basic understanding of human color perception.

1.4 Flies as a Model for Color Vision

While studies in higher brain regions of primates and more complex animals are hindered by exceedingly intricate processing mechanisms, simple model organisms are poised to provide clarity in the field of color vision studies. Opponent signals have been measured across the animal kingdom, reinforcing the importance of this operation across evolution, and strengthening the case to study these color circuits in a variety of species. The idea that simple brains are capable of encoding color has existed since the early 1900s, when Karl Von Frisch demonstrated that honey bees can discriminate between colors [36]. We now know that a large variety of arthropods are capable of color vision. There have been an extensive number of behavioral color vision studies in bees and

butterflies (reviewed in [37]), but lack of genetic tools has prevented depth of understanding of the neural circuits underlying these behaviors.

Drosophila melanogaster has emerged as a genetically tractable system to study circuit level mechanisms of color vision [38-43], and color opponent signals have been measured at the axonal terminals of cone-like photoreceptors in the fly brain [38]. Moreover, flies have demonstrated stereotyped behaviors that indicate that these animals do indeed utilize chromatic information at the behavioral level. Flies demonstrate spectral preference for shorter wavelengths [40, 42-44], which in itself indicates that phototactic behavior in *Drosophila* is not achromatic. Moreover, even though *Drosophila* strongly prefer UV light, mixed UV and visible light presented to flies gives rise to phototactic inversion: an inhibitory effect that depresses phototactic behavior [45]. This behavioral opponency is likely the behavioral output of underlying color opponent mechanisms which compare UV and visible light at the cellular level (see next paragraph). In addition, flies can discriminate between wavelengths in the blue-green range [39]. This behavior is independent of intensity, providing evidence for a comparison of blue and green in the fly brain.

The fruit fly possesses cone-like photoreceptors R7 and R8, which ultimately enable the fly to achieve the aforementioned color-dependent behaviors. Unlike the 2D lattice photoreceptor arrangement found in mammals, the light-sensing rhabdomeres of R7 and R8 are positioned one on top of

another [46] (Figure 1A). This architecture allows photoreceptors in each optical unit, or ommatidium, to absorb photons emanating from the same point in visual space. A specialized circuit taking advantage of this configuration was recently described to generate color opponent signals through reciprocal inhibition between pairs of R7 and R8 photoreceptors from a single ommatidium [38], allowing for pixel-by-pixel comparison of wavelengths. Because of the spectral composition of the fly eye, these intra-ommatidial interactions impose specific constraints on the types of spectral comparisons that the circuit can make. There are two types of ommatidia in the main part of the fruit fly eye that are distributed in a stochastic pattern (65% ‘‘yellow’’ and 35% ‘‘pale’’; Figures 1A and 1D; reviewed in [47]). Pale ommatidia express the short-UV-sensitive Rh3 rhodopsin in R7 and the blue-sensitive Rh5 in R8. Yellow ommatidia express the long-UV-sensitive Rh4 rhodopsin in R7 and the green-sensitive Rh6 in R8. An opponent mechanism purely based on intra-ommatidial interactions therefore defines two separate color opponent channels, both comparing spectral information along a UV versus visible axis.

This architecture has the advantage of potentially allowing chromatic information to be extracted at the full resolution of the eye, similarly to achromatic pathways driven by R1–R6 photoreceptors [48], which express the broadband opsin Rh1 (Figures 1A and 1D). However, it does not allow for additional comparisons to be made in the spectral domain, such as those

between the blue and green part of the spectrum, which appear to be used behaviorally [39, 41, 43] and which may be beneficial in terms of efficient signal processing. Lateral interactions between R7s and R8s from neighboring ommatidia, akin to those mediated by horizontal cells in the mammalian retina [14], would allow for increased resolution of chromatic pathways in the spectral domain and provide the fly with more flexible mechanisms for encoding chromatic information. In the following chapters, I investigate these circuit mechanisms of photoreceptor opponency in detail. In addition, I start to explore how early chromatic circuits adapt to myriad environmental conditions, and how opponent signals propagate to downstream circuits.

Figure 1: Experimental Setup and Stimulus Design

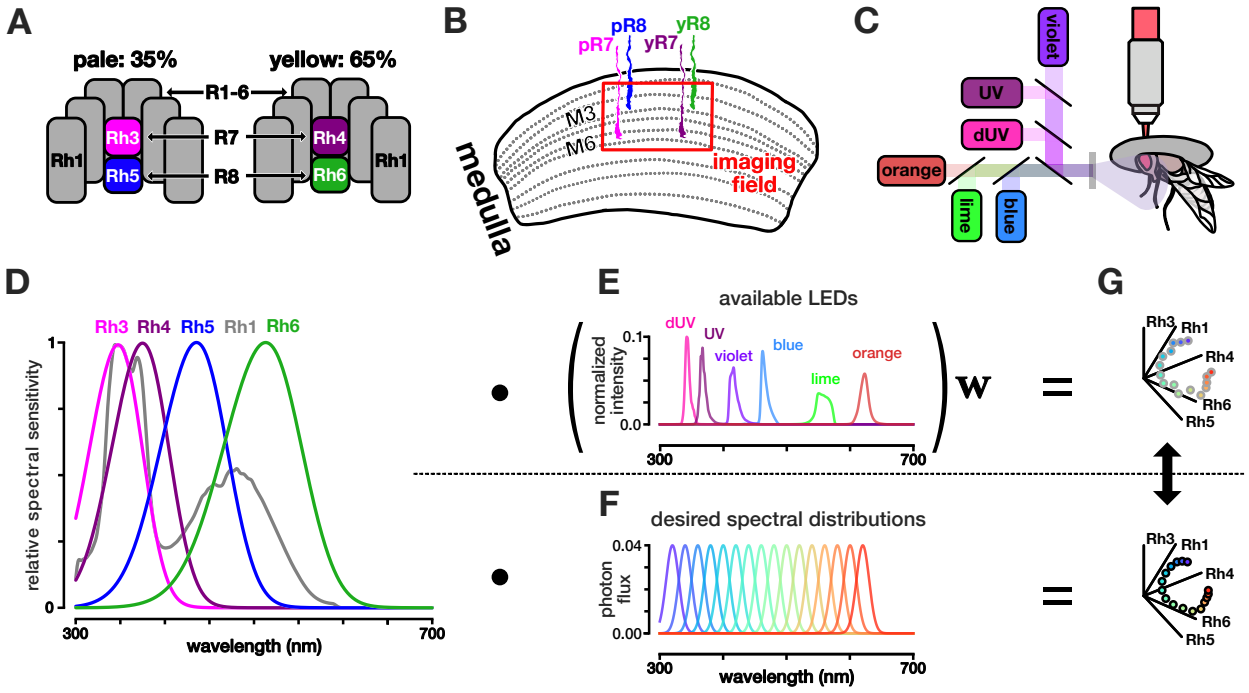

(A) Spectral composition of pale and yellow ommatidia of the Drosophila eye. Pale ommatidia express Rh3 and Rh5 in R7 and R8, respectively. Yellow ommatidia express Rh4 and Rh6 in R7 and R8, respectively. R1–R6 all express Rh1. (B) Photoreceptors in Drosophila project from the retina into the optic lobe. My imaging experiments target the axon terminals of R7 and R8 in the medulla at the level of layers M6 and M3, respectively. (C) Two-photon imaging setup. The fly is secured facing LED setup, and LED sources are combined using a custom color mixer to form a single collimated beam. (D) Relative spectral sensitivity of opsins expressed in the fruit fly retina; data from [49] and fitted with equation from [50]. (E) Normalized photon flux across the wavelength spectrum, corresponding to the various LEDs used for stimuli. (F) Desired set of spectral distributions to test to build a spectral tuning curve. (G) For any given single wavelength in (F), the relative photon capture is calculated (q) for all five opsins by integrating over the opsin sensitivities in (D) and plotting a vector in photon capture space. Single wavelengths are then simulated with combinations of the available LEDs in (E) that most closely recreate that vector. See also Figure 2.

Chapter 2: Circuit Mechanisms Underlying Chromatic Encoding in Drosophila Photoreceptors

2.1 Introduction

Color vision is an important source of visual information, enhancing my recognition of objects in complex visual fields. How is wavelength information extracted by the brain? A single type of photoreceptor cannot distinguish wavelength independently of the intensity of light because different spectral distributions of varying intensity can give rise to the same photoreceptor output [3]. Generally, color percepts can only be extracted by comparing the output from at least two photoreceptors with different spectral sensitivities. This comparison is apparent in color opponent neurons, which receive antagonistic inputs from different photoreceptor types and therefore exhibit opposing responses to different ranges of wavelengths [51]. Understanding of the neural processes that lead to our perception of colors therefore critically depends on our understanding of color opponent signals and the underlying circuits that establish them. Moreover, opponent processing motifs extend to other sensory systems, such as olfaction [52], which further highlights the importance of unraveling this type of antagonistic signaling in the more general context of sensory processing.

Here, I measure the spectral tuning of all four types of wavelength-specific photoreceptors in the fly visual system. I find that each R7 and R8

photoreceptor type displays specific and distinct wavelength opponent properties, which cannot be explained solely by previously described reciprocal inhibition within single ommatidia. At the circuit level, I show that indirect antagonistic interactions between R7s and R8s from neighboring ommatidia also contribute to shaping the spectral tuning of all photoreceptor outputs and that these interactions are mediated by the horizontal-cell-like medulla interneuron Dm9. Moreover, indirect interactions enable additional comparisons in the spectral domain that correspond to efficient decorrelation and dimensionality reduction of the spectral sensitivities of *Drosophila* opsins. In addition, my colleague builds a linear recurrent model constrained by the underlying circuit interactions. This model accurately predicts my observed responses while also showing that electron-microscopy-based synaptic count provides an accurate proxy for synaptic weight in this early processing step in color circuits. Finally, our circuit model predicts a receptive field for R7 and R8 outputs with a broadband surround superimposed on a color opponent center, combining the motifs of both an evolutionarily convergent circuit architecture and an insect-specific visual circuit.

2.2 Results

R7 and R8 Inputs Are Transformed into Opponent Outputs through Interactions between Photoreceptor Types

Color opponent responses are established via antagonistic interactions of inputs from different types of photoreceptors. In the case of Drosophila photoreceptors R7 and R8, rhabdomeric responses of these photoreceptors in the eye can be considered inputs, and their color opponent axonal responses in the medulla can be considered outputs (Figure 3A). To understand how inputs are combined to give rise to color opponent outputs, my first goal was to measure and compare the rhabdomeric and the axonal spectral tuning properties of these photoreceptors.

In vivo two-photon imaging of genetically targeted GCaMP6f in R7 and R8 photoreceptors allows for straightforward measurement of their axonal outputs in the M6 and M3 layers of the medulla, respectively (Figure 1B). However, I could not visualize rhabdomeres in the eye with my imaging setup and could therefore not directly measure rhabdomeric responses. Instead, I used genetic tools to make indirect measurements of putative rhabdomeric responses. Because these responses are transformed into axonal outputs through interactions with other photoreceptor types [38], I reasoned that measurements at the axonal level in mutant flies where these interactions are abolished can be considered equivalent to putative rhabdomeric responses. For this set of

experiments, I isolated these responses in mutant flies where only the imaged photoreceptor type is active, effectively preventing external inhibitory input from other photoreceptor types. This is done by functionally rescuing phototransduction in single photoreceptor types in the blind *norpA* mutant background by driving expression of upstream activating sequence (UAS)-NorpA with Rhodopsin-Gal4 drivers [53].

In order to compare putative rhabdomeric and axonal tuning, our lab developed a method to measure spectral tuning curves (Figures 1D–1G). Specifically, I measured neuronal responses to a range of relatively narrow-band light sources of equal photon flux (E = moles of photons per m^2 per s) spanning the fly's visible spectrum. Instead of using a system with a large number of different light sources, our lab developed a method that allowed me to measure tuning curves using only a limited number of light-emitting diodes (LEDs). For a given light source, each photoreceptor type will ''capture'' a specific number of photons. This number, or photon capture, is calculated as a function of each opsin's sensitivity and the spectrum of the light source [54, 55] (see Methods; Equation 5). I simulated the effect of this particular light source on the fly eye by showing a combination of the six LEDs in my stimulus setup, which evoked the same capture in each of the five photoreceptor types as the intended narrow-band light source (see Methods and Figure 2 for details on implementation and accuracy). All experiments were performed in light-adapted

conditions where the simulated light source is presented over a background light. Measuring responses to these simulated light sources across the spectrum allowed us to construct spectral tuning curves for a given cell type.

Figure 2. Contributions of Individual LEDs to Simulations of Various Wavelengths

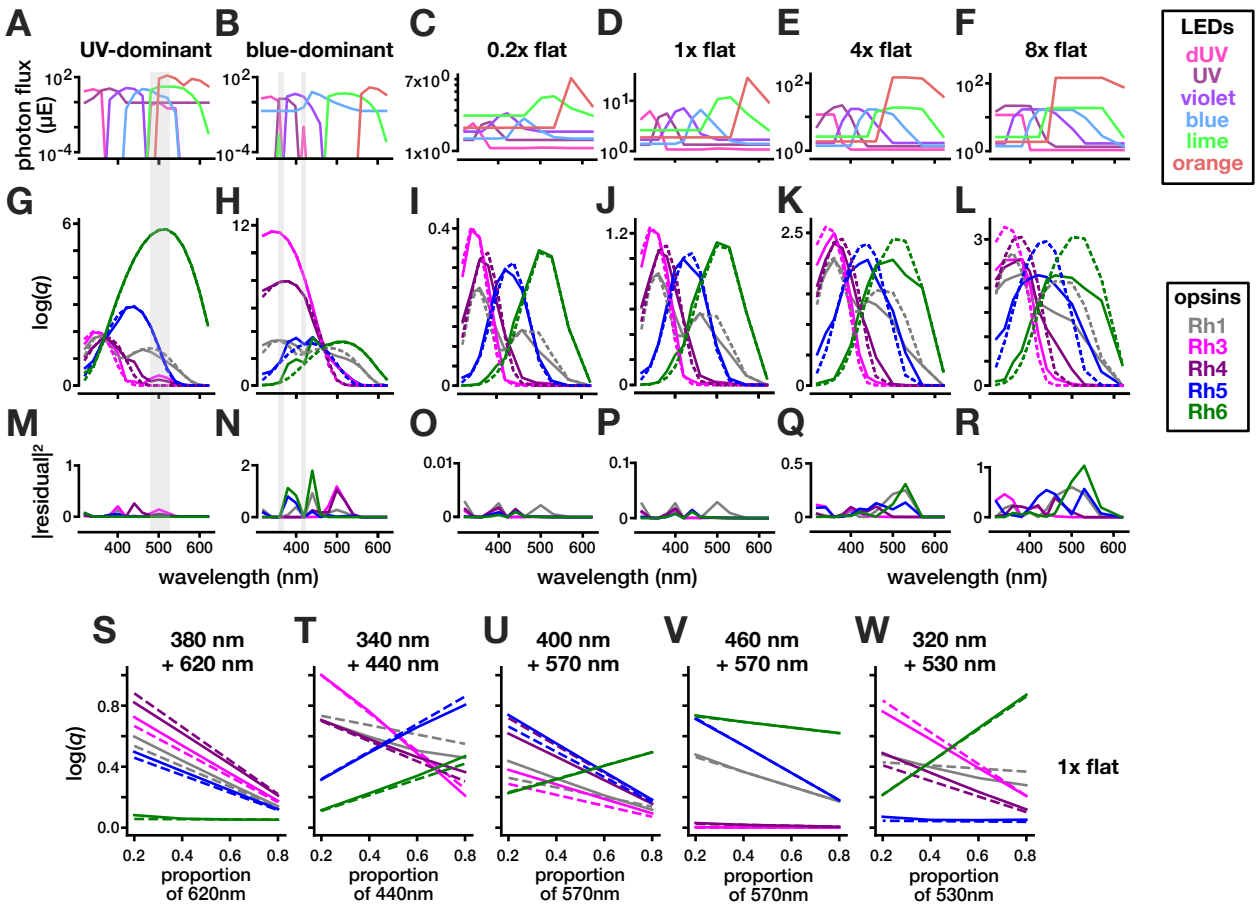

(A-F) Relative photon flux of each of the 6 LEDs in the stimulation set-up used to simulate wavelengths across the spectrum for stimuli in the UV-dominant, blue-dominant, or flat background. G-L. Target log(q) of each opsin for a given simulated wavelength (dashed line) and log(q) of the best fit using our experimental setup (solid line) (see methods; Equation 7). (M-R) The squared residuals calculated for target wavelengths and fitted wavelengths for all stimuli. The gray vertical shaded area in the UV- and blue-dominant background indicate wavelengths that are discarded when plotting spectral tuning curves. (S-W) Target log(q) of each opsin for a given mixture of wavelengths (dashed line) and log(q) of the best fit using my experimental setup (solid line) (see methods; Equation 7 and Equation 8).

As expected from the spectral sensitivities of the opsins they express, the putative rhabdomeric responses I measured show UV sensitivity in p/yR7 peaking at 360 nm and 380 nm, respectively; blue sensitivity in pR8 peaking at 420 nm; and blue/green sensitivity in yR8 peaking at 500 nm (Figures 3B– 3E, see Figures 4 and 5 for two-photon imaging details). These neural responses are directly related to spectral sensitivities of the opsins that these photoreceptors express. It was previously shown that a logarithmic transformation of photon capture corresponds to the transformation of light absorption of a photoreceptor by the phototransduction cascade [56, 57]. I thus compared the tuning curves I obtained to the log of the relative photon capture log(q) in each rhodopsin, specifically calculated for the presented stimuli. I found that the measured tuning curves closely match the calculated log(q). This result shows that log(q) is a reliable estimate of the putative rhabdomeric responses I measured in this system, and I will subsequently refer to log(q) as the calculated rhabdomeric response.

In the case of axonal responses in wild-type flies, I measured spectrally opponent waveforms in all photoreceptor types (Figures 3F–3I). pR7 outputs are activated by UV spanning 320–420 nm and inhibited by longer wavelengths (Figures 3F and 3J). yR7 outputs are also activated by UV, with their response remaining excitatory up to 440 nm and becoming inhibitory from 480 nm onward (Figures 3G and 3K). pR8 outputs are the only ones to show a tri-lobed spectral

tuning (Figures 3H and 3L). They are activated by blue light ranging from 400 to 500 nm and inhibited by UV ranging from 320 to 380 nm, as well as in the green from 530 to 620 nm. yR8 outputs are activated by wavelengths covering the wide range of 400–620 nm in the blue/green but inhibited by UV from 320 to 380 nm (Figures 3I and 3M).

Each R7 and R8 terminal type thus displays distinct and specific wavelength opponent properties that are dependent on interactions between photoreceptors with different spectral sensitivities. This is generally consistent with previous work. Schnaitmann et al. [6] found that opponent signals at the level of R7 and R8 outputs are generated through both direct and indirect antagonistic interactions between pairs of R7 and R8 photoreceptors from a single ommatidium: direct interactions in the form of reciprocal histaminergic inhibition and indirect, inhibitory interaction mediated by a yet-to-be-identified medulla interneuron. However, I measured opponency in ranges that are not predicted by reciprocal inhibition exclusively between R7 and R8 photoreceptors from the same ommatidium. This is most obvious in the case of pR7 and pR8. Indeed, both of these photoreceptor types are inhibited by green light (>540 nm; Figures 3F and 3H), whereas my measurements of their putative rhabdomeric responses show that neither responds at these long wavelengths (Figures 3B and 3D). Intra-ommatidial interactions (between R7 and R8 from the same ommatidium) alone are therefore not sufficient to explain these properties.

Figure 3. R7 and R8 Putative Rhabdomeric Responses Are Transformed into Opponent Outputs

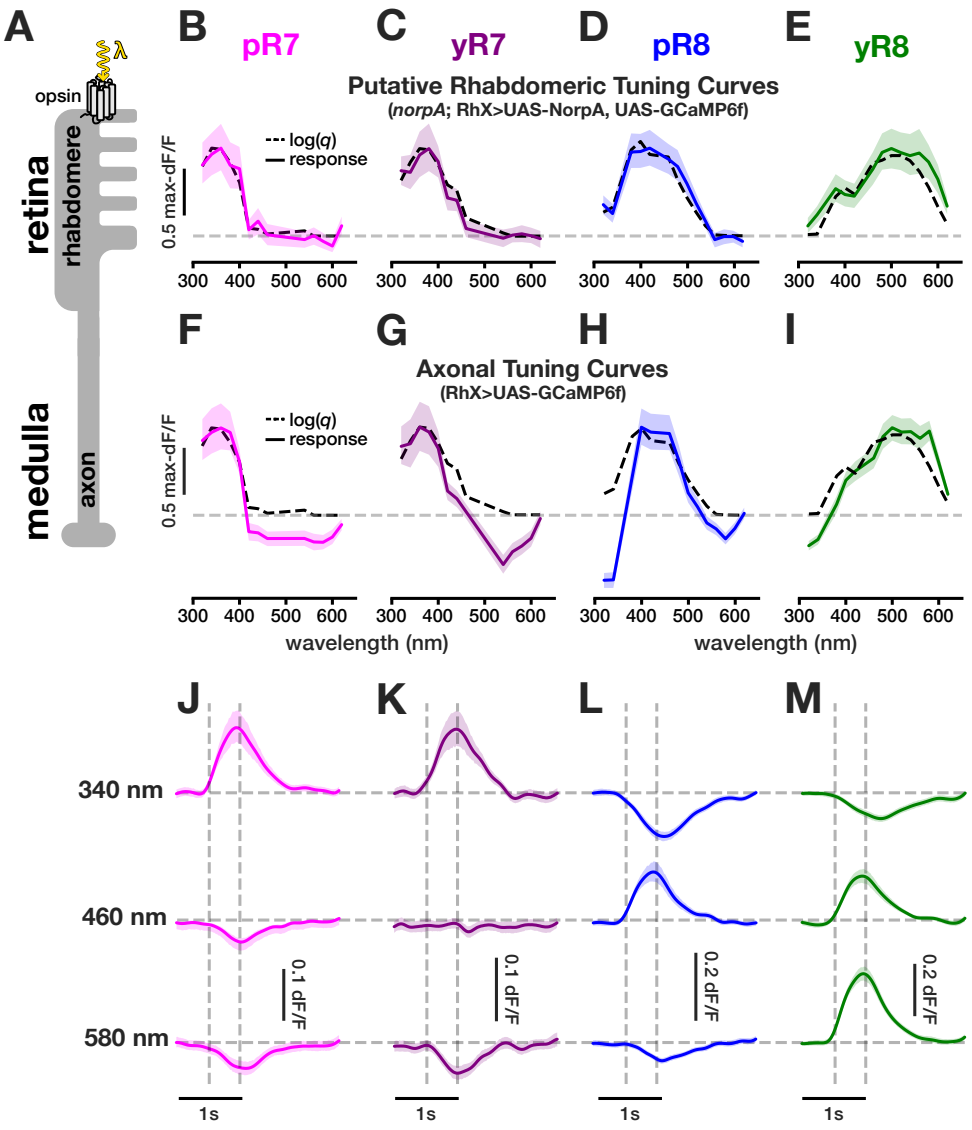

(A) In Drosophila photoreceptors, light (λ) is absorbed in the retina by rhodopsin molecules at the level of the rhabdomeres, where phototransduction takes place. Photoreceptors project their axons to the medulla where synaptic interactions occur. (B–E) NorpA, an essential component of the phototransduction cascade, was restored in *norpA* blind flies in individual photoreceptor types (RhX denoting Rh3/4/5/6). This allowed for measurement of putative rhabdomeric spectral tuning in photoreceptor axons by eliminating interactions from other cell types. Max-normalized responses of R7/R8 axons were measured across simulated wavelengths to construct spectral tuning curves. (B), (C), (D), and (E) refer to pR7, yR7, pR8, and yR8 tuning curves, respectively. Regions of interest (ROIs) correspond to individual cells, whose responses

were averaged equally across flies. n = 106 ROIs (8 flies), 96 (8), 69 (7), and 26 (4), respectively. Dashed black lines represent the log(q). Colored lines represent the mean photoreceptor response. Shaded region represents the 95% confidence interval. Dashed gray lines represent baseline fluorescence. (F–I) Max-normalized spectral tuning curves constructed using the amplitudes of measured responses of R7 and R8 axons in wild-type flies. (F), (G), (H), and (I) refer to pR7, yR7, pR8, and yR8 tuning curves, respectively. n = 152 (8 flies), 134 (6), 138 (7), and 129 (6), respectively. (J–M) Average GCaMP6f responses of R7 and R8 axons in wild-type flies to 0.5s flashes of three simulated wavelengths. Vertical dashed gray lines represent onset and offset of light presentation. (J), (K), (L), and (M) refer to pR7, yR7, pR8, and yR8 responses, respectively.

Figure 4. Representative ROI Detection and Responses in R7 and R8.

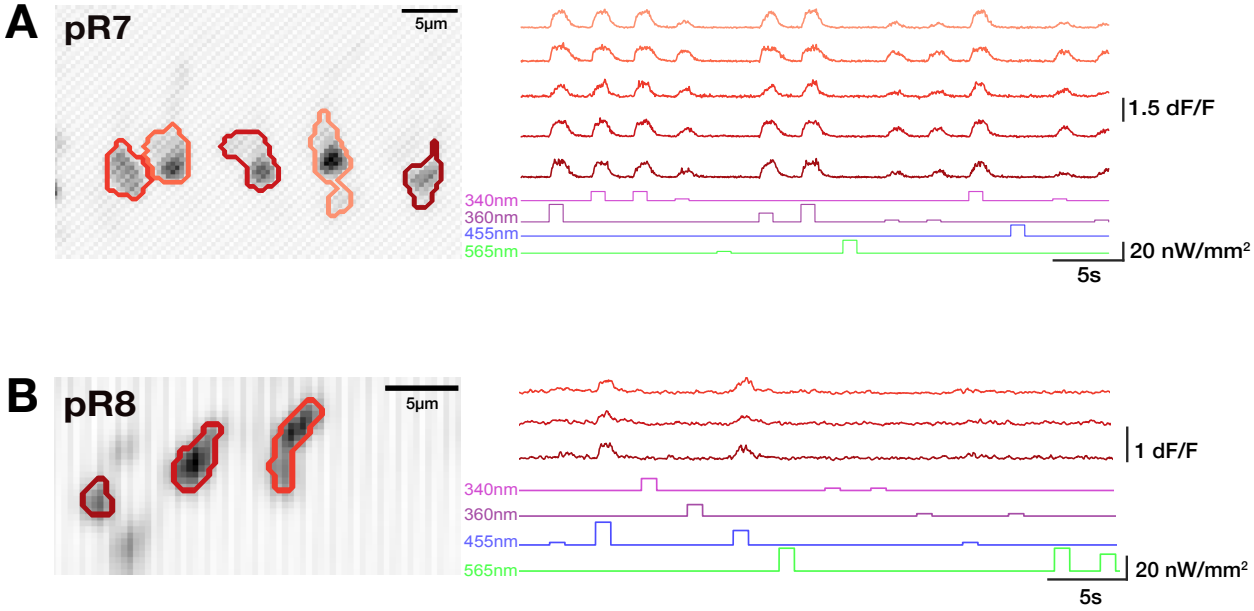

(A-B) ROIs of pR7 and pR8 axons respectively in the medulla, and GCaMP6f responses measured in these ROIs to randomized 1s flashes of varying wavelengths/intensities of light.

Figure 5. Raw GCaMP6f Calcium Responses in R7 and R8.

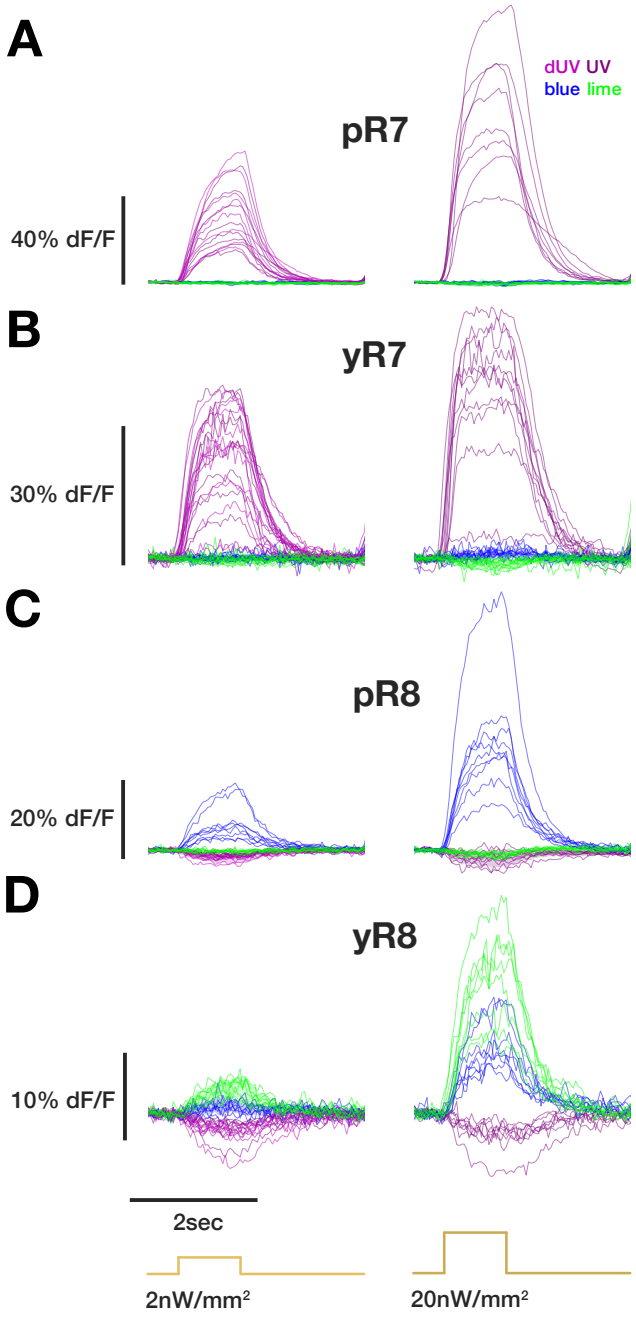

(A-D) Visualization of responses in single flies to various wavelengths/ intensities of light in R7 and R8 axons.

To eliminate the possibility that differing stimulus regimes elicited these divergent results, I performed additional experiments in pR7 and pR8 in which I simultaneously presented full-field steps from two light sources, consistent with the methods of Schnaitmann et al [6]. I presented both an LED step that most closely matched the preferred wavelength ranges of pR7 and pR8 (UV and blue LED, respectively), along with an additional step from a second LED type. (Figure 6). Consistent with the results of Schnaitmann et al, the pR7 response to UV was reduced when paired with a blue step, and the pR8 response to blue was reduced when paired to a UV step Figure 6A, D). However, my results diverge in that pR7 and pR8 clearly show a decreased response to their preferred LED when paired with green or orange LED Figure 6B-C, E-F). These decreased responses confirm opponency in the >540 nm range, in pR7 and pR8 as was previously shown in the spectral tuning curves I measured. This result supports the conclusion that inter-ommatidial interactions contribute to opponency at the level of photoreceptors.

Armed with this discovery, I next aimed to further define the circuit mechanisms that combine and process R7 and R8 signals to give rise to the diverse, spectrally opponent axonal responses that I measured.

Figure 6. pR7 and pR8 Responses to Their Preferred Wavelengths are Reduced by Simultaneous Presentation of Other Colors

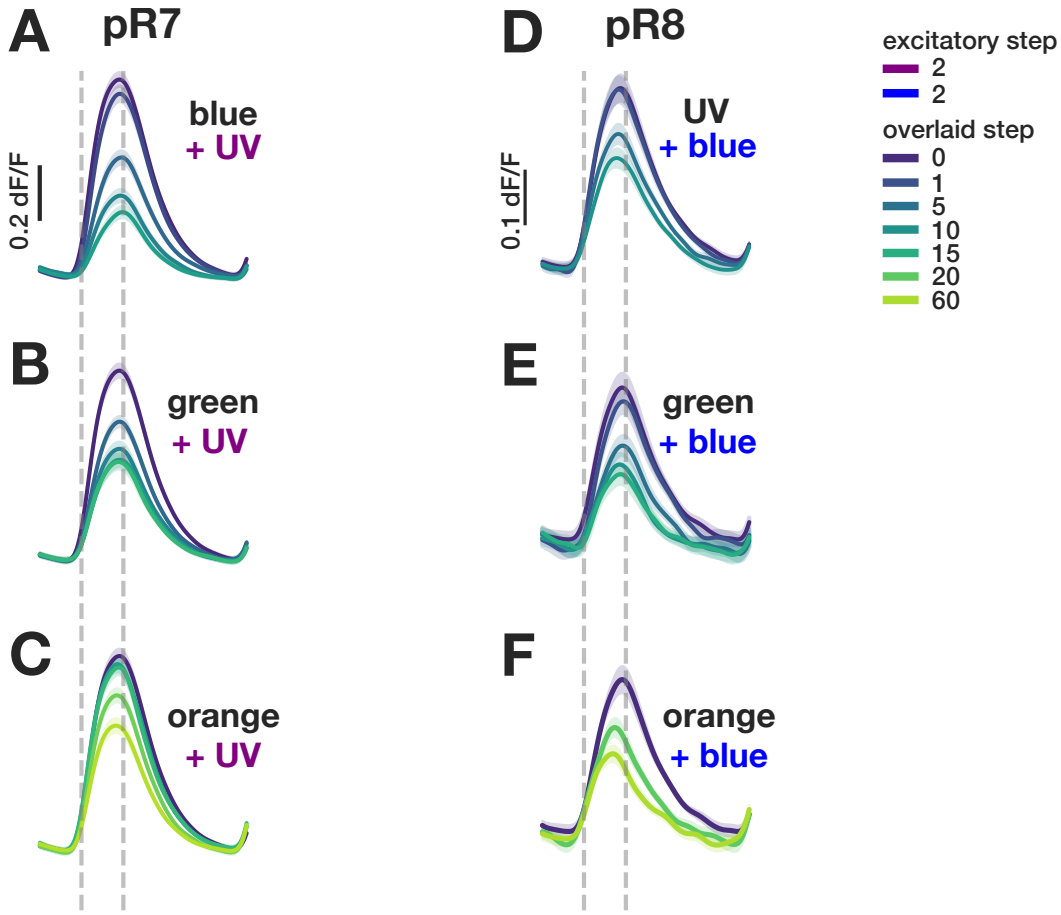

pR7 and pR8 responses to simultaneous 0.5s full-field flashes of UV at 2uE and varying intensities of blue (A), green (B), and orange (C), and UV (D), green (E), and orange (F), respectively. Grey dashed line represents the onset and offset of stimulus presentation. N = 5 flies for both genotypes.

Both Intra- and Inter-ommatidial Antagonistic Interactions Shape the Spectral Tuning Properties of R7 and R8 Outputs

According to my putative rhabdomeric measurements (Figures 3B–3E), the inhibition measured in pR7 and pR8s axons in the long-wavelength range can only originate from yR8 or the broadband photoreceptors R1–R6. Thus, I hypothesized that inter-ommatidial interactions (between R7s and R8s from neighboring ommatidia) and/or inputs from R1–R6 contribute to the spectral tuning of R7 and R8 outputs. I employed genetic methods to determine the contribution of specific photoreceptor types to the spectral tuning of R7 and R8 outputs. I took advantage of *norpA* mutants and selectively rescued NorpA in pairwise combinations of photoreceptor types.

First, I imaged pR7 in flies in which pR7 function was restored in combination with one other photoreceptor subtype. The tuning curve of pR7 in flies when phototransduction is rescued in both pR7 and pR8 is similar to that of wild-type pR7 in that there is activation in the UV range (320–400 nm) and inhibition in the blue range (420–460 nm; Figure 7B). This is consistent with intra-ommatidial inhibition from pR8, as the putative rhabdomeric responses of pR8 show blue sensitivity (Figure 3D). However, inhibition is lost in the long wavelengths (>540 nm). In contrast, in a pR7/yR8 rescue, the tuning curve for pR7 displays clear inhibitory responses at all wavelengths above 420 nm (Figure 7C), showing that yR8 contributes to blue/green inhibition in pR7 through inter-

ommatidial interactions. In a pR7/yR7 rescue, pR7s are inhibited in the UV/blue range (400–450 nm; Figure 7A), showing that yR7s contribute to pR7 responses. These results demonstrate that, in addition to intra-ommatidial interactions from pR8, inter-ommatidial interactions from both yR8 and yR7 contribute to opponent responses measured in pR7.

I performed the same set of experiments while imaging pR8 terminals. In a pR8/pR7 rescue, the tuning curve of pR8 becomes bi-lobed, showing inhibition only in the UV range (<360 nm) and not in the green wavelength range (>540 nm; Figure 7D). Conversely, in a pR8/yR8 rescue, pR8 still shows inhibition to green, but not to UV (Figure 7F). In a pR8/yR7 rescue, I did not see strictly inhibitory responses under my recording conditions, but I did observe a statistically significant decreased response in pR8 in the UV range (300–340 nm) in comparison to the calculated rhabdomeric response (Figure 7E). This indicates that yR7 has an inhibitory effect on pR8. These results show that, similarly to pR7s, both intra-ommatidial and inter-ommatidial interactions contribute to the opponent responses measured in pR8s.

Figure 7. Pairwise NorpA Rescues Highlight Sources of Opponency in R7/R8

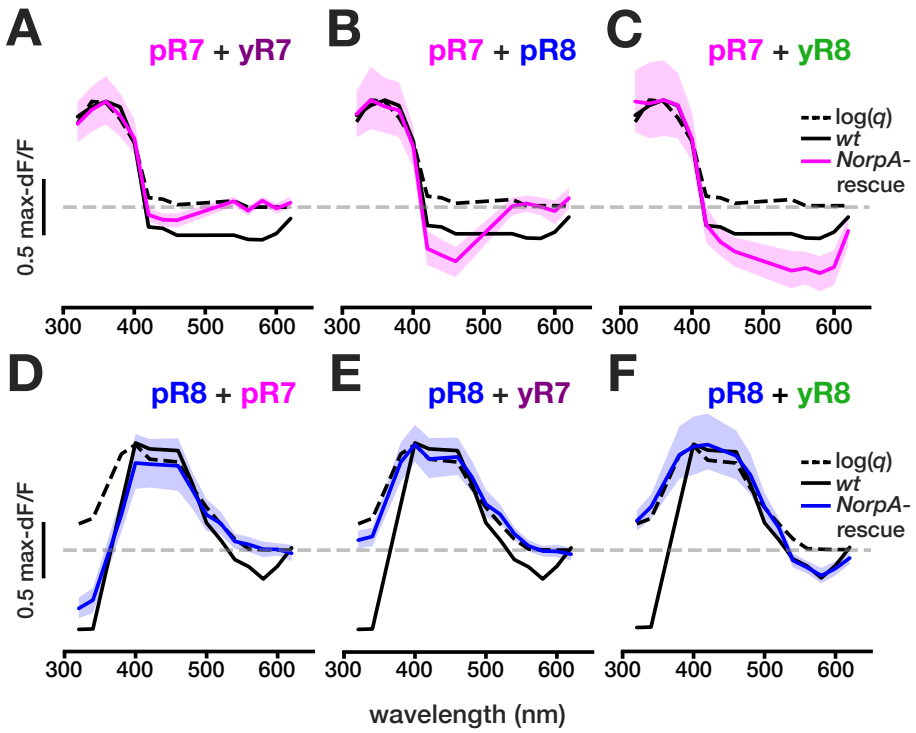

NorpA, a component of the phototransduction cascade, was restored in *norpA* blind flies in select pairs of photoreceptor types to determine contributions to opponency. (A–C) Max-normalized responses of pR7 axons were measured across simulated wavelengths, with NorpA restored in pR7 and a second indicated photoreceptor type. (A), (B), and (C) refer to pR7 responses in flies where pR7 is rescued in conjunction with pR8, yR7, and yR8, respectively. n = 106 ROIs (8 flies), 108 (8), 132 (8), and 104 (6), respectively. Dashed black lines represent log(*q*), black lines represent the wild-type response, colored lines represent the mean photoreceptor response, shaded regions represent the 95% confidence interval, and dashed gray lines represent baseline fluorescence. (D–F) Max-normalized responses of pR8 axons were measured across simulated wavelengths, with NorpA restored in pR8 and a second indicated photoreceptor type. (D), (E), and (F) refer to pR8 responses in flies where pR8 is rescued in conjunction with pR7, yR7, and yR8, respectively. n = 63 (7 flies), 80 (9), 69 (7), and 63 (7), respectively. See also Figure 8 and Table 1.

I next measured responses in all rescue combinations for yR7 and yR8. In experiments where yR7 was imaged, I confirmed antagonistic inputs from its intra-ommatidial partner yR8 in the green range (>540 nm) but could not detect significant inhibition from pR8 or pR7 (Figures 6A–6D). yR8 imaging confirmed antagonistic inputs from both p and y R7s in the UV range (<380 and <400, respectively), but no significant inhibition from pR8 was detected (Figures 6E–6H).

Lastly, I investigated the possible contribution of R1–R6 to the wild-type signals by rescuing NorpA in R1–R6 in conjunction with each individual R7/R8 photoreceptor type. I found no significant differences in paired rescues with R1–R6 compared to the measured putative rhabdomeric responses (Figures 6I– 6P) and thus did not consider R1–R6 contributions further in my analysis.

Together, these experiments demonstrate that inhibitory interactions between R7 and R8 are not confined within medulla columns. Rather, there is a larger set of interactions between columns in the medulla that shape the tuning of R7 and R8 outputs, adding both additional spectral comparisons and a spatial dimension to opponent pathways.

Figure 8. Combinations of NorpA Rescues Show Interactions Between R7 and R8, but not R1-6

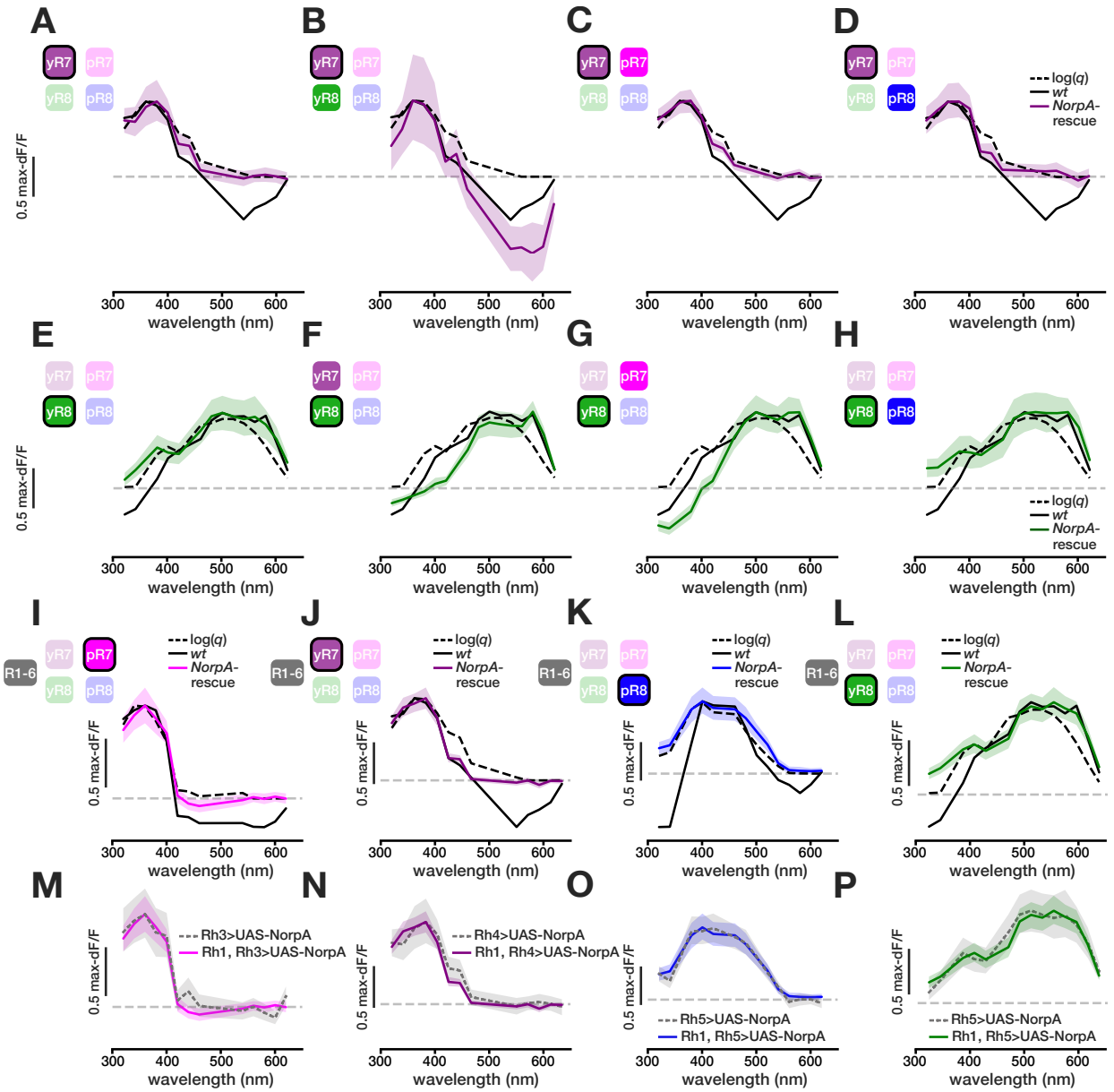

(A-D) Max-normalized responses of yR7 axons with NorpA restored in *norpa* blind flies in yR7 alone, or in yR7 and the indicated photoreceptor type. Ns= 132 ROIs (8 flies), 96(8), 135(12), and 51(5), respectively. Dashed black lines represent log(q), black lines represent the wild type response, colored lines represent the mean photoreceptor response, shaded regions represents the 95% confidence interval, dashed grey lines represent baseline fluorescence. E-H. Max-normalized responses of yR8 axons with NorpA restored in *norpa*- blind flies in yR8 alone, or in yR8 and the indicated

photoreceptor type. Ns= 126(6), 74(5), 48(6) and 26(4), respectively. I-L. Max-normalized responses of each photoreceptor axon type with NorpA restored in *norpa*-blind flies in select pairs of photoreceptor in the imaged photoreceptor and R1-6. (Ns= 150(6), 103(5), 85(7) and 95(4), respectively. M-P. Comparison of max-normalized spectral tuning curves of the single NorpA rescues (small dashed grey lines) and NorpA restored in the imaged photoreceptor and R1-6 (colored lines) showing no significant difference.

The Horizontal-Cell-like Dm9 Neuron Mediates Lateral, Indirect Opponency

The fact that opponent responses in R7s and R8s are shaped by inhibitory interactions between pale and yellow ommatidia is reminiscent of the circuit architecture of vertebrates, where horizontal cells mediate center-surround inhibitory interactions [17]. I thus hypothesized that inter-ommatidial inhibition in the fly medulla is similarly mediated by a horizontal-cell-like interneuron in the circuit. The medulla interneuron in question should fulfill the following requirements: (1) be both pre- and postsynaptic to p/yR7s and p/yR8s; (2) span multiple columns (R2) in the medulla; and (3) be excitatory, to enable opponent interactions through relief of excitation. Based on electron microscopy (EM) and RNA-sequencing (RNA-seq) studies, the only neuron that fits these criteria is the horizontal-like cell Dm9 (Figure 9A) [58-61].

Dm9 is a multi-columnar medulla interneuron, spanning an average of seven columns and occupying distal medulla layers M1–M6 (Figures 9B, 9C, 10A, and 10B). These cells tile in layers M2–M5 but overlap in M1 and M6 [62]. EM reconstructions show a large number of synapses from R7 and R8 onto to Dm9, as well as synapses from Dm9 back to both R7 and R8. In addition, Dm9s receive indirect inputs from R1 to R6 through the lamina monopolar cell L3, as well as inputs from the amacrine cell Dm8 [58, 61]. Dm9 has been proposed to be an excitatory glutamatergic neuron [59].

To test whether Dm9 is functionally connected to photoreceptors, my colleagues and I optogenetically activated Dm9 using CsChrimson [63] while simultaneously imaging the activity of UV-sensitive R7s. The experiments were done in *norpA* blind flies to avoid the effects of activating the wild-type opsins themselves. During CsChrimson activation using a red LED (660 nm), I observed depolarization of R7 photoreceptors in the experimental flies and not in the control flies (Figure 9D), thereby confirming a functional excitatory connection between Dm9 and photoreceptors.

Next, I measured the spectral tuning of Dm9. I found that Dm9 is inhibited by a broad range of wavelengths spanning the whole spectrum (Figures 9E–9H). This is consistent with EM data showing that Dm9 gets inputs from all photoreceptor types. In addition to inhibition to light ON, Dm9 responds positively to light OFF, especially at high intensities of the stimulus. It is unclear how this OFF response arises. However, based on connectivity, it could result from L3 inputs [64].

I then silenced the activity of Dm9 by expressing the inward- rectifying potassium channel Kir2.1 in these neurons specifically while imaging from pR8 axons. I chose this particular photoreceptor type because it provides the clearest readout of the effect of intra- or inter-ommatidial interactions. UV inhibition in pR8 is likely a combination of intra- and inter-ommatidial interactions, although long-wavelength inhibition is due to inter-ommatidial

interactions only. I therefore expected only a partial loss in UV opponency after Dm9 silencing, because direct intra-ommatidial inputs from pR7 should not be affected. Conversely, I expected complete loss of inhibition at the long wavelengths with complete Dm9 silencing, as I have shown that the source of these signals is purely inter-ommatidial. I found that when Dm9 activity is inhibited, inhibition in pR8 is overall reduced compared to the spectral tuning in wild-type flies, and pR8 tuning is no longer tri-lobed (Figures 9I and 10C). These terminals still show opponency in the UV range (300–340 nm) compared to the calculated rhabdomeric response. However, opponency is lost in the green-wavelength range (>500 nm). This result is consistent with Dm9 mediating inter-ommatidial interactions.

In addition to these silencing experiments in pR8, I tested the role of Dm9 in this circuit by disrupting feedforward inhibition from photoreceptors to Dm9 specifically. Schnaitmann et al. [38] showed that direct axo-axonal inhibition is mediated by the histamine receptor HisCl1. As medulla neurons express the Ort histamine receptor and not HisCl1 [59], histaminergic transmission to medulla neurons (including Dm9) must be mediated by Ort. As expected, in an *ort*, *HisCl1* double-mutant background, I could not detect any inhibition in pR8 photoreceptors (Figures 9J and 10D). I then rescued Ort expression exclusively in Dm9 neurons in this mutant background (Figure 9J). When imaging pR8 in these conditions, I found restored opponent waveforms both in the UV range

(300–340 nm) and the green range (>500 nm), showing that Dm9 is sufficient for mediating inter-ommatidial antagonism.

I then performed these silencing and rescue experiments in pR7, which also exhibits long-wavelength opponency potentially mediated by Dm9. Surprisingly, in flies where Dm9 is silenced, opponency in pR7 is lost in the 400–480 nm range, but remains at wavelengths >480 nm (Figure 10E). Thus, either there is an additional interneuron specifically involved in R7 indirect opponency or the Dm9 silencing was incomplete. The latter is more likely, as electron microscopy reconstructions have not identified other neurons with the adequate wiring. Thus, future experiments in which Dm9 is imaged directly to measure the extent of silencing will be crucial to determine this. I next tested whether Dm9 would be sufficient for opponency in pR7. As expected, in an *ort, HisCl1* double-mutant background, I could not detect any inhibition in pR7 photoreceptors (Figure 10F). I then rescued Ort expression exclusively in Dm9 neurons in this mutant background. When imaging pR7 in these conditions, I found restored opponent waveforms both in blue-green range (>400 nm)(Figure 10F). This shows that Dm9 is sufficient for mediating interommatidial antagonism in pR7.

As there is evidence that Dm9 is glutamatergic [59], and I found that there are functional excitatory connections between Dm9 and photoreceptors (Figure 9D), it is likely that feedback from Dm9 onto R7 and R8 is mediated by

glutamate receptors. To test if glutamate signaling underlies indirect opponency in photoreceptors, I created flies in which EKAR, an ionotropic glutamate receptor expressed in R7 and R8 [59], was knocked down. I measured spectral tuning in pR8 in these EKAR knockdown flies (Figure 10G). As expected, due to the remaining HisCl1-mediated intra-ommatidial opponency, I found that pR8 still shows opponency in the UV range (300–340 nm). However, opponency is largely lost in the green-wavelength range (>500 nm), with the exception of slight inhibition remaining at 580nm. As long-wavelength opponent signals in pR8 are due to inter-ommatidial interactions (Figure 7), this result indicates that indirect opponency in photoreceptors is largely mediated by glutamate signaling through EKAR receptors. As there is no evidence for excitatory neurotransmitter expression in Dm9 aside from glutamate, the remaining opponency at 580nm could remain due to incomplete knockdown of EKAR, or involvement of additional interneurons.

Altogether, these data combined with known connectivity indicate that the horizontal cell Dm9 mediates indirect intra- and inter-ommatidial inhibitory interactions. However, I observed an incomplete loss of inter-ommatidial opponency in pR7 after Dm9 silencing, and an incomplete loss of inter-ommatidial opponency in pR8 after EKAR knockdown. Thus, putting potential methodology pitfalls aside, it is possible that other cell types in the medulla may be also be involved in mediating this indirect opponency. The interneuron in

question must be both pre- and post-synaptic to R7 and R8, as our lab has previously shown that these are the sources of indirect opponency for one another [65]. Unfortunately, electron microscopy data does not give us many clues, as Dm9 remains the single obvious candidate for these interactions. However, it is important to note that medulla reconstructions only span 7 columns, and thus cannot capture tangential cells with wider reaching projections. Thus, there may be unidentified tangential neurons in the medulla that are potentially involved in inter-ommatidial opponency.

Figure 9. The Horizontal-Cell-like Interneuron Dm9 Mediates Indirect Spectral Opponency

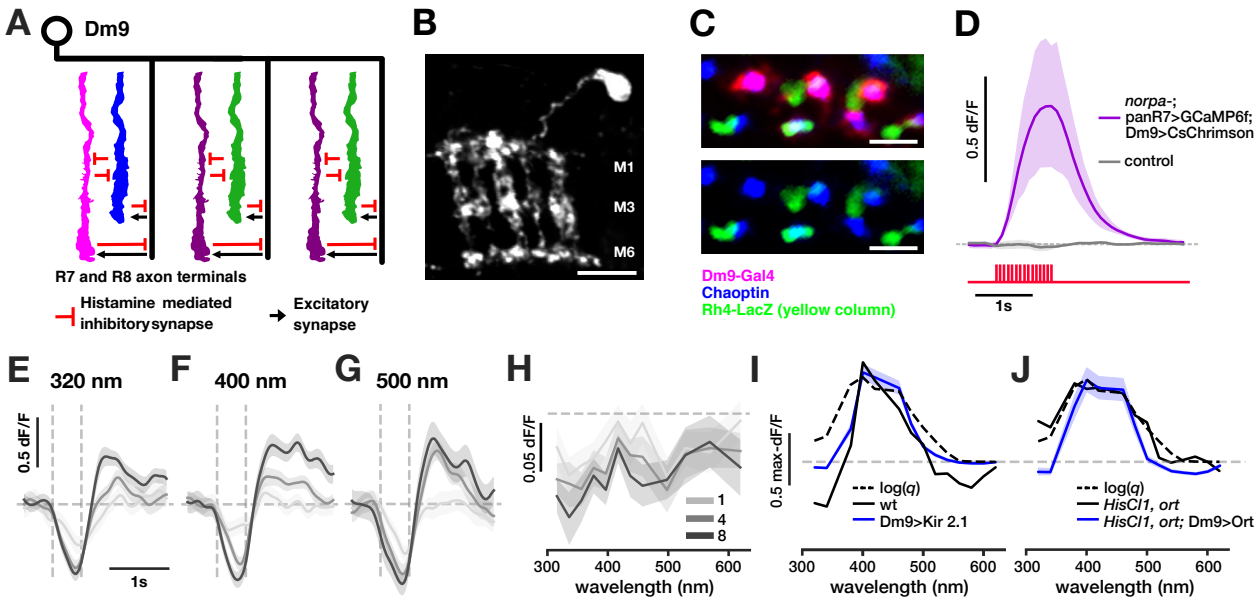

(A) Schematic of Dm9/photoreceptor connectivity. Dm9 is an excitatory interneuron spanning multiple medulla columns shown to be both pre- and postsynaptic to R7/R8. (B) Side view of a maximum projection of a single Dm9 clone (R32E04-Gal4). Scale bar: 10 mm. (C) Cross section view of a single Dm9 clone (pink), photoreceptor terminals (blue), and yR7 terminals (green) shows a single Dm9 contacts both yellow and pale ommatidia. Scale bars: 5 mm. (D) Purple trace represents GCaMP6f responses in R7 after a pulse train of red light in flies expressing CsChrimson in Dm9 (R32E04 driver) n = 37 (4 flies). Gray trace represents R7 responses in control flies without CsChrimson expression. n = 70 (5 flies). Solid lines represent the mean; shaded region represents 95% confidence interval. Vertical red lines represent light presentation. Horizontal dashed gray lines represent baseline fluorescence. (E–G) Responses of Dm9 (R32E04-Gal4) to 0.5-s flashes of three simulated wavelengths over a 10-mE background with a flat spectrum. (E), (F), and (G) refer to Dm9 responses to 320 nm, 400 nm, and 500 nm stimuli, respectively. Responses to three luminant multiples of each wavelength are shown (13, 43, and 83). Solid lines represent the mean; shaded region represents 95% confidence interval. Vertical dashed gray lines represent onset and offset of light presentation. Horizontal dashed gray lines represent baseline fluorescence. (H) Dm9 spectral tuning curves corresponding to three luminant multiples of each wavelength are shown (13, 43, and 83). (I) pR8 max-normalized spectral tuning curves. Blue line represents pR8 responses in a Dm9-silenced background (R32E04-Gal4 driving UAS-Kir2.1) n = 323 ROIs (6 flies). Black line represents wild-type pR8 responses using the same GCaMP6f construct. Dashed black lines represent the log(*q*). (J) pR8 max-normalized spectral tuning curves. Blue line represents pR8 tuning in a *HisCl1*, *ort* mutant background, where Ort was rescued in Dm9 (R21A12- GaL4 driving UAS-Ort) n = 153 (6 flies). Black line represents pR8 in a *HisCl1*, *ort* mutant background. Dashed black lines represent the log(*q*).

Figure 10. Immunolabeling of Dm9 and pR8/pR7 Spectral Tuning Curves for Various Mutant Backgrounds

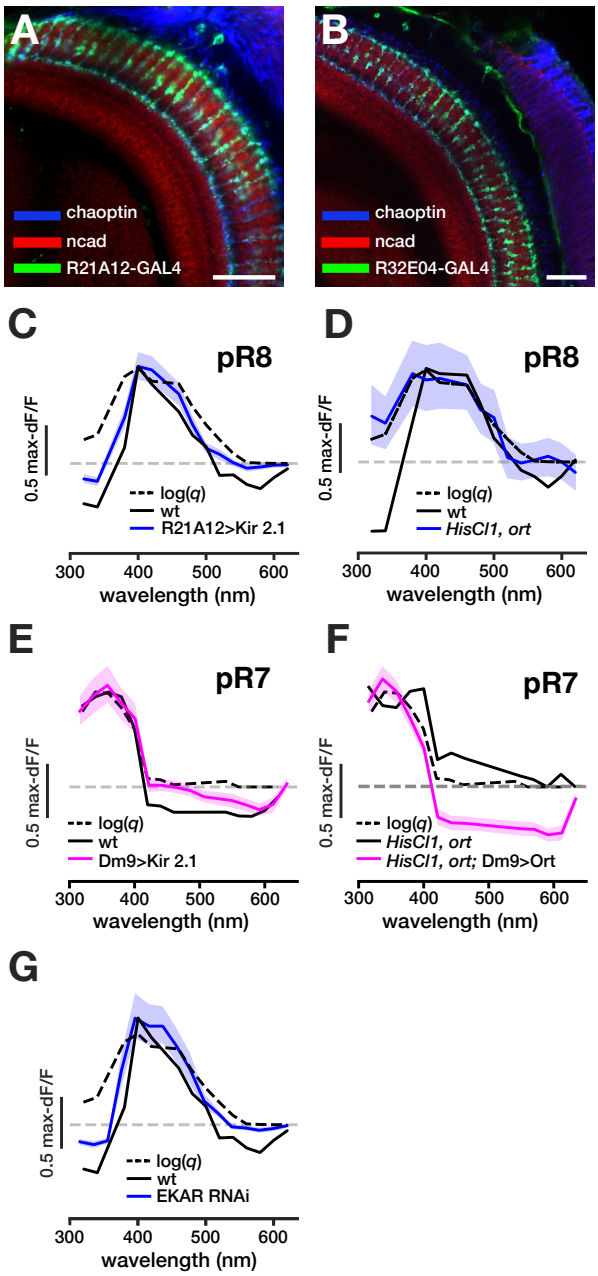

(A) The optic lobe of the fruit fly stained for Dm9 (R21A12-Gal4, green), the neuropil (Ncad, red), and photoreceptor axons (Chaoptin, blue). Scale bar, 30 *μm*. (B) The optic lobe of the fruit fly stained for Dm9 (R32E04-Gal4, green), the neuropil (Ncad, red), and photoreceptor axons (Chaoptin, blue). Scale bar, 30 *μm*. (C) pR8 max-normalized spectral tuning curve when silencing Dm9 using the R21A12-Gal4 line N= 158 ROIs (5

flies). The black line represents the wild type response using the Rh5-LexA line. The dashed black line represents log(q). The shaded region represents the 95% confidence interval for the given spectral tuning curve. (D) pR8 max-normalized spectral tuning curve in a *hiscl-, ort-* mutant N= 153 (10). The black line represents the wild type response. (E) pR7 max-normalized spectral tuning curve when silencing Dm9 using the R21A12-Gal4 line (N= 1). The black line represents the wild type response using the Rh5-LexA line. The dashed black line represents log(q). The shaded region represents the 95% confidence interval for the given spectral tuning curve. (F) pR7 max-normalized spectral tuning curves. Blue line represents pR7 tuning in a *HisCl1*, *ort* mutant background, where Ort was rescued in Dm9 (R21A12- GaL4 driving UAS-Ort) (N=7). Black line represents pR7 in a *HisCl1*, *ort* mutant background. Dashed black lines represent the log(q). (G) pR8 max-normalized spectral tuning curve in an EKAR knockdown (N=2).

Histamine Receptor Contributions to R7 and R8 Spectral Opponency

As previously mentioned, R7 and R8 express the histamine receptor HisCl1, which has been shown to underlie direct axo-axonal opponency in these photoreceptors [38]. Conversely, medulla neurons express the Ort histamine receptor instead, which has been shown to mediate indirect opponency [38, 59, 65]. However, there is conflicting data describing to what extent each of these receptor types is necessary and/or sufficient for these types spectral opponency in R7 and R8 [38, 65]. To gain further insight into receptor contributions, I measured R7 and R8 spectral tuning in both *ort* and *Hiscl1* mutant backgrounds. I performed two-photon calcium imaging while presenting stimuli that span the wavelength spectrum, as described previously [65]. In *HisCl1* mutants, R7s and pR8s retain spectral opponent properties (Figure 11 A-D) (yR8 *Ort* mutant data not available). This is largely consistent with previous data and circuit models, as Ort-mediated opponency could explain the opponent waveforms in all of these cells[38, 65]. In *Ort* mutants, yR7 retained opponency in the similar ranges as wild type flies (>450nm) (Figure 11B). This was expected, as HisCl1-mediated opponent signals from yR8 were still intact. In yR8 however, opponency was eliminated (Figure 11D). This is consistent with measurements made by Schnaitmann et. al, who find that opponency to UV in yR8 is lost in *Ort* mutants [38]. Surprisingly, both pR7 and pR8 retained opponent waveforms in

the *Ort* mutant background (Figure 11 A,C). This is particularly unexpected at longer wavelengths, as opponency in this range originates from yR8 input [65]. Because yR8s are spatially separate from pR7 and pR8, long-wavelength opponency in these cells necessitates indirect interactions through medulla interneurons, which exclusively express Ort [38, 59, 65]. Moreover, I have previously shown that silencing Dm9 eliminates long-wavelength opponency in pR8, and Dm9 has been shown to only express the Ort histamine receptor [65]. Thus, the fact that green opponency remains in pR7 and pR8 in an *Ort* mutant was unexpected. This could possibly be explained by a genetic compensation in *Ort* mutants in which HisCl1 is derepressed in Dm9 and/or additional medulla cells. Lastly, as expected, opponency was shown to be eliminated in all photoreceptor types imaged in the *ort, Hiscl1* double mutants (Figure 11 E-G).

Figure 11. Histamine Receptor Contributions to R7 and R8 Spectral Opponency

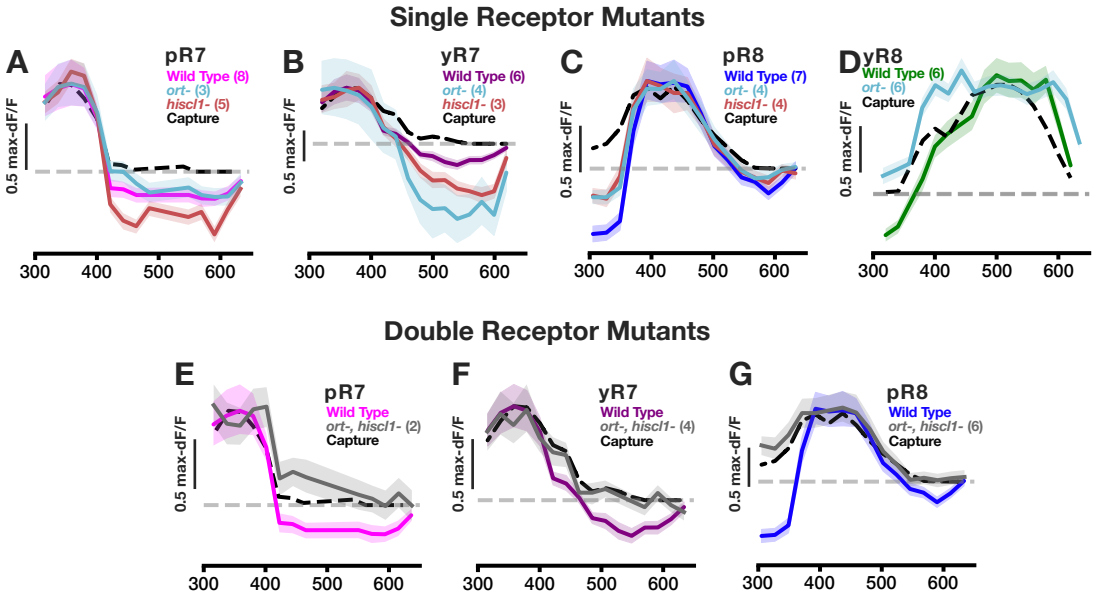

(A–D). Average responses of R7 and R8 axons to simulated wavelengths in mutants for both the Ort and Hiscl1 histamine receptors. Magenta, purple, dark blue and green lines (respectively) represent wild-type pR8 responses using the same GCaMP6f construct. Black dashed line represent the log(q). Grey dashed line represents baseline (E–G). Same as (A–D), but with flies mutant for both Ort and Hiscl1 receptors.

Opponent Mechanisms Produce an Efficient Representation of Chromatic Information at the Level of R7 and R8 Outputs

Our data show that inter-ommatidial antagonism, along with previously described intra-ommatidial antagonism, shape the responses of the outputs of R7 and R8 photoreceptors. What are the consequences of this dual circuit on spectral encoding?

A clear consequence of opponency is a narrowing of the tuning of photoreceptor responses in the medulla compared with their calculated rhabdomeric responses. To quantify this, I acquired an additional dataset of spectral tuning measurements, in which measurements for all photoreceptor types were made with the same stimulus over a large range of intensities and combinations of single wavelengths (Figure 12). I used a flat background spectrum at an intensity of 10μE, where photon flux was consistent across all wavelengths, and presented full field steps of luminant multiples ranging over several orders of magnitude.

Figure 12. R7 and R8 Spectral Tuning to Stimuli Presented Over a Flat Background Spectrum

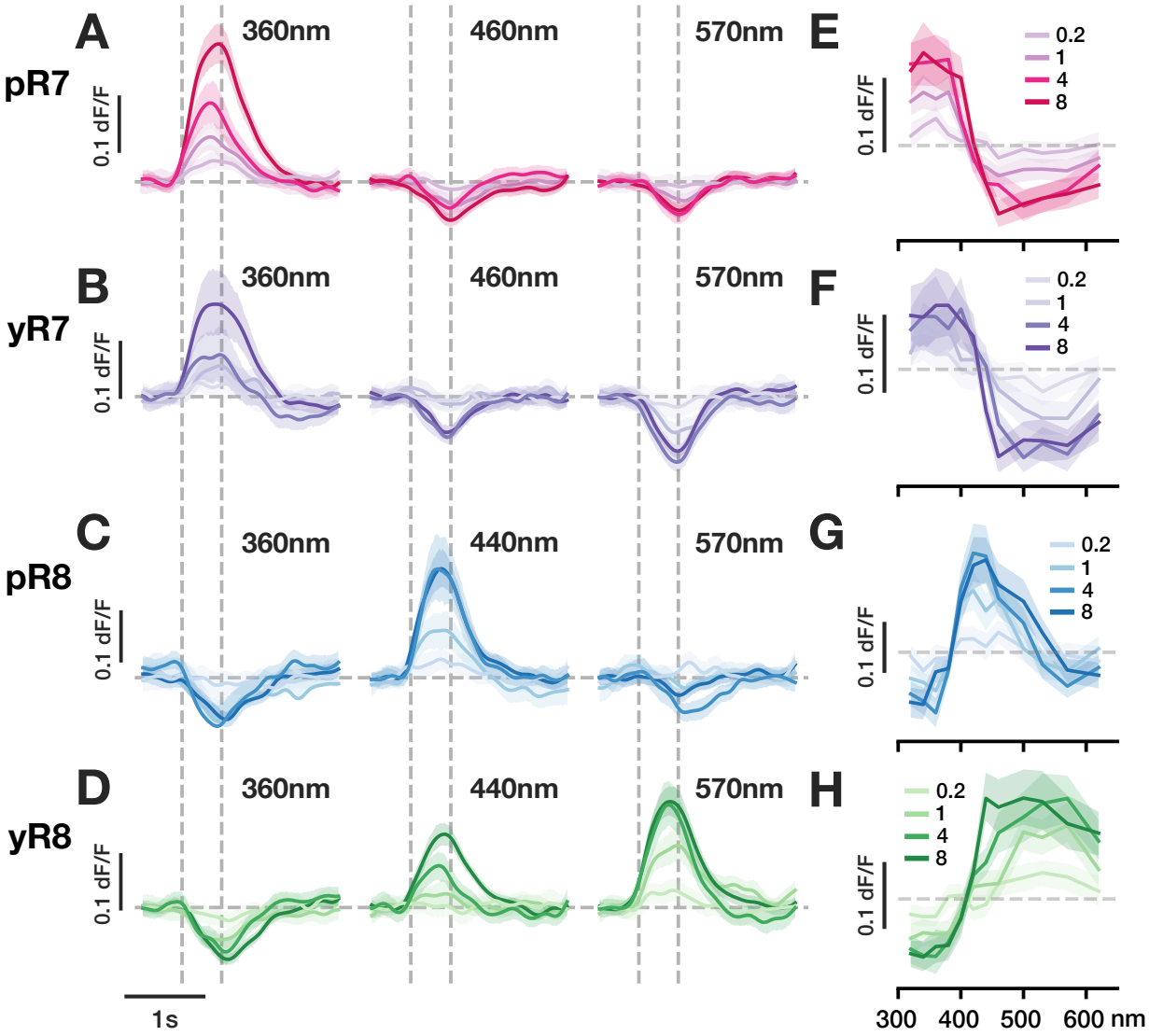

(A–D) Average GCaMP6f responses of R7 and R8 axons in wild type flies to 0.5 second flashes of three simulated wavelengths over the flat background. Solid lines represent the mean, shaded region represents 95% confidence interval. Colored lines represent stimuli of four different luminant multiples. (E–H) Tuning curves constructed using the amplitudes of measured responses of R7 and R8 axons from across the wavelength spectrum.

The opponent waveforms under these conditions are consistent with my wavelength-dominant background experiments. My colleagues and I calculated correlation coefficients between the calculated rhabdomeric responses of R7 and R8 photoreceptors (Figure 13A) and between their measured axonal responses (Figure 13B). As expected from the high degree of overlap between the spectral sensitivities of the four opsins expressed in R7 and R8 (Figure 1D), there is a high degree of correlation between the calculated rhabdomeric responses. This effect is particularly pronounced for spectrally consecutive opsins, such as Rh3 and Rh4 (0.97), Rh4 and Rh5 (0.82), and Rh5 and Rh6 (0.79). However, after antagonistic interactions have occurred in the medulla, I find that axonal responses of the different photoreceptor types become decorrelated (yR8 and pR8; yR7 and pR8) and, in some cases, anti-correlated (pR7 and both R8s; yR7 and yR8).

The responses measured at the level of photoreceptor outputs vary along two main axes: one that compares UV and visible wavelengths (y/pR7s and yR8) and one that compares blue and UV + green wavelengths (pR8). Can these two axes of opponency produce an efficient representation of the chromatic information detected at the retinal level? Inspired by the Buchsbaum and Gottschalk [24] study in humans, my colleagues and I performed principal-component analysis (PCA) to ask whether these axes preserve the chromatic

information conveyed by R7 and R8 photoreceptors while also decorrelating the inputs (Figures 13C and 13D). The first principal component (PC) is achromatic, with equal loading for all opsin types, and it accounts for over half of the variance. Higher PCs therefore describe variance in the chromatic domain. The second PC opposes the two R7 opsins and the two R8 opsins, corresponding to comparison between the UV and the visible parts of the spectrum (Figure 13E). The third PC opposes Rh5 and Rh3 + Rh6, which corresponds to a comparison between blue and UV + green (Figure 13F). The last PC opposes Rh3+Rh5 and Rh4+Rh6. The first two chromatic PCs together with the achromatic PC explain 97% of the variance. Interestingly, these two chromatic PCs broadly describe the two types of responses I measure at the output of R7 and R8: UV versus visible (observed in pR7/yR7 and yR8) and blue versus UV + green (observed in pR8; Figures 13E and 13F). The first chromatic axis is supported by intra-ommatidial interactions, whereas the second chromatic axis necessitates inter-ommatidial interactions. Therefore, by aligning with these two axes, the opponent mechanisms not only efficiently decorrelate chromatic signals but also retain maximum chromatic information while reducing the overall dimensionality of the inputs.

Figure 13. Opponency Is Consistent with Principal Components that Efficiently Decorrelate and Preserve Chromatic Information

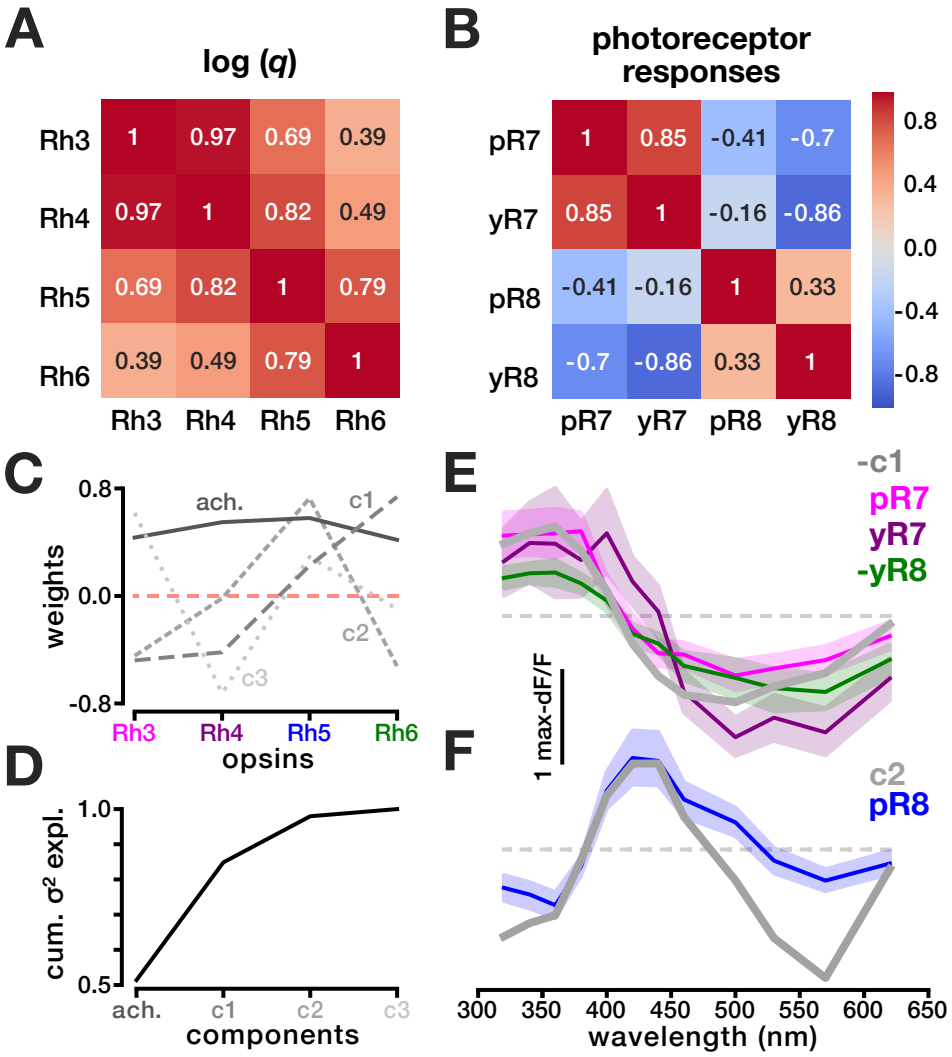

(A) Correlation matrix comparing the calculated rhabdomeric responses of R7s and R8s. (B) Correlation matrix comparing the measured axonal responses in R7 and R8 outputs. (C) Decomposition of opsin spectral sensitivities using principal-component analysis (PCA) yields four main principal components: an achromatic component (ach) and three chromatic components (c1, c2, and c3). (D) Percentage of the variance explained by each principal component. (E and F) Comparisons between the max-normalized tuning curves based on the measured tuning curves in R7 and R8 axons (colored lines) and the first two chromatic components c1 and c2 (gray lines) to the flat background for luminant multiple 4.

A caveat of this analysis is that it assumes a flat spectrum, which does not take into account reflectances in naturalistic scenery. Thus, a more biologically relevant context can be achieved by using a set of natural stimulus spectra which spanning the relevant wavelength range of fruit flies (300–600 nm; Figure 14A). In this case, PCA on all four opsin channels reveals similar principal components as in the case of a flat spectrum. This finding indicates that, across conditions, my observed opponent responses are close to the optimal decorrelation of input signals using PCA (Figures 13B and 13C). This consistency across conditions fits with the idea that one function of this circuit is to remove correlations in the input signals, which mainly arise from the overlap of the opsin sensitivities rather than the composition of the spectrum.

Figure 14. PCA on Calculated Photon Captures of R7s and R8s to a Set of Hyperspectral Reflectances.

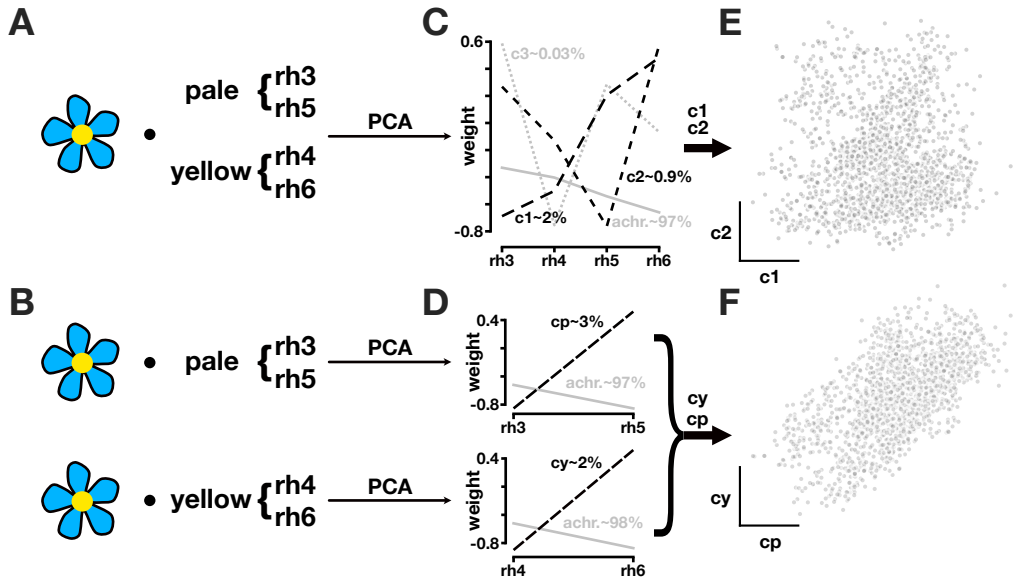

(A) Schematic of principal component analysis on R7 and R8 channels. Flower graphic represents the naturalistic hyperspectral reflectances. (B) Obtained principal components, each marked with its associated explained variance. achr.: first PC (achromatic); c1: second PC (chromatic component 1); c2: third PC (chromatic component 2); c3: fourth PC (chromatic component 3). (C) Hyperspectral reflectances projected onto the PCs c1 and c2. (D) Schematic when performing PCA on yellow and pale ommatidia separately. (E) Obtained principal components, each marked with its associated explained variance, when performing PCA on yellow and pale ommatidia separately. achr.: first PC for both pale and yellow ommatidia (achromatic); cy: second PC for yellow ommatidia (chromatic component); cp: second PC for pale ommatidia (chromatic component). (F) Hyperspectral reflectances projected onto the PCs cy and cp.

A Recurrent Model of Early Color Circuits Predicts Spectrally Opponent R7 and R8 Outputs

I next asked whether the circuit architecture we identified and tested experimentally can quantitatively reproduce the opponent responses we measure in R7 and R8 outputs. Before constructing a model, my colleagues and I wanted to test the linearity of the system. Specifically, we asked if the photoreceptor axonal outputs are linear with regard to their rhabdomeric inputs (i.e. $\log(q)$). To test for linearity, we assessed two empirical measures: scalar invariance and additivity. The estimated zero-crossing points of the opponent tuning curves of R7s/R8s do not significantly change at different intensities of light measurements, showing scalar invariance within the bounds of our recording conditions (Figure 15A). To test for additivity, I measured the responses of photoreceptor outputs to five wavelengths combinations: 340/440 nm, 380/620 nm, 400/570 nm, 460/570 nm, and 320/530 nm (measured at four different mixing ratios, Figure 15 B-F). We then compared the responses to corresponding linear additions of the single wavelength responses (see Methods; Equation 8). The measured responses to the mixtures (filled circles) do not significantly differ from the linear predictions (shaded area) (Figure 15 B-F). Therefore, the circuit under investigation behaves linearly within the range of stimuli used in this study.

Because photoreceptors integrate rhabdomeric inputs linearly, we first performed a linear regression without biological constraints (Methods; equation 11). We used the calculated rhabdomeric responses as independent variables to fit our amplitude measurements in the flat background condition. We found that comparisons between measured axonal responses and estimated responses based on linear regression fall on the unity line (Figure 15 G-J), thus providing a good fit. The unconstrained linear regression provides a benchmark for our model, which includes biological circuit constraints.

Interestingly, linear regressions that include intra-ommatidial R7/R8 opsin pairs together with at least one additional opsin type provide better fits than when exclusively considering intra-ommatidial R7/R8 opsin pairs as independent variables (Figure 15 K-N). This is most obvious in the case of pR7 and pR8. These regressions are consistent with findings that both intra- and inter-ommatidial interactions shape opponent responses in R7/R8.

Figure 15. Measured Responses in R7 and R8 Axons in the 10 µE Background Result from Linear Combinations

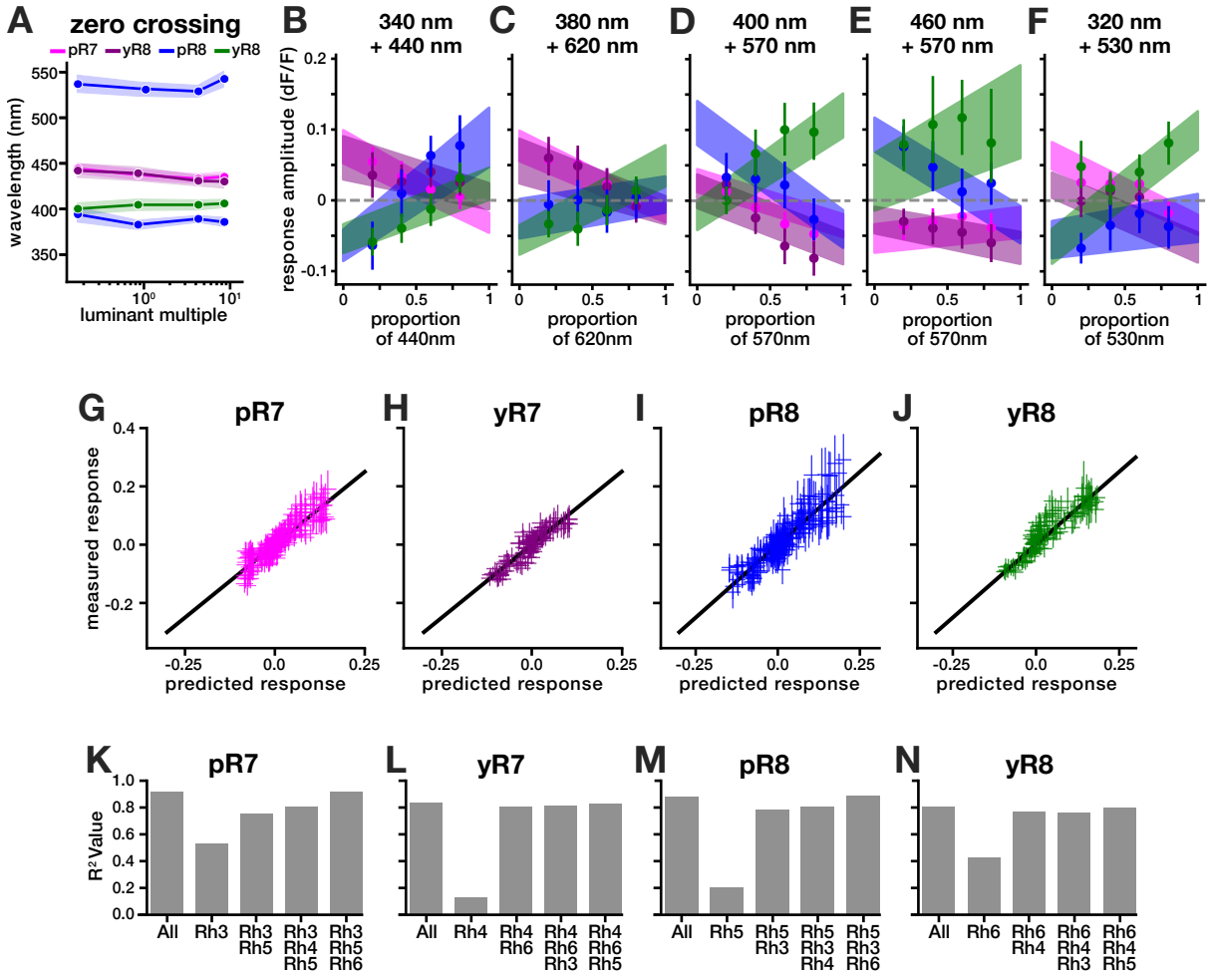

(A) The estimated zero crossing points of the measured tuning curves in each R7/R8 photoreceptor. As pR8's tuning curve has a trilobed form, it crosses the zero axis twice. (B–F) Measured responses of R7 and R8 axons to mixed combinations of different wavelength stimuli (filled circles) compared to the linear prediction of responses to those stimuli (shaded region) (see methods; Equation 8). (G–J) 4-fold cross-validated linear regression using the log of the relative photon capture of Rh3–6 and responses measured at the level of R7 and R8 outputs. (K–N) R2 values when using varying opsin contributions in linear regressions to predict opponent responses in R7s and R8s.

Because photoreceptors integrate inputs linearly, my colleague Matthias Christenson built a linear recurrent network constrained by the circuit connectivity and synaptic signs (see Methods, Equation 12). The overall architecture of the network consists of direct inhibitory connections between photoreceptors within a single ommatidium and indirect connections via the excitatory interneuron Dm9. Dm9 receives inhibitory inputs from all four photoreceptors and feeds back onto all photoreceptors. We fit the steady state of this model to our measured amplitudes (see Methods, Equation 14). We then further constrained the model by using synaptic counts obtained by EM reconstructions as a proxy for synaptic weights[60, 66], and included fitted gain parameters for each of the photoreceptors and Dm9 separately.

As a control, we replaced the weights in our model with randomly drawn sample weights 10,000 times and created a distribution of R^2 values. We found that using the synaptic count for our weights results in a significantly better performance than when using random weights. Therefore, the synaptic count data retrieved from EM give a non-random estimate of input strength to photoreceptors.

We used our model to predict the full-field spectral filtering properties of each photoreceptor (Figure 16A). These filtering properties reflect our experimental tuning curves but also predict the response of photoreceptors to arbitrary spectral distributions. Finally, we modeled the sensitivities of the

center and the surround separately (Figure 16B). As expected, we found that sensitivities in the center are bi-lobed in all cases, corresponding to comparisons between the UV part of the spectrum and the visible part. Additionally, we found that the sensitivities of the surround are broadband and strongest between 350 nm and 500 nm. The predictions made by our model lay the groundwork for future experiments, in which spatially patterned stimuli can be used to further explore how this circuit processes information both spatially and spectrally.

To start to test this model experimentally, I first aimed to determine the extent of opponency in the spatial dimension. I devised a spatially patterned stimulus to test for center-surround organization of photoreceptor receptive fields, which is predicted by our model. Using a digital light processing projector, I presented drifting sinusoidal gratings of varying spatial frequency onto a screen in front of wild type flies while performing two-photon imaging in yR8 axons. Using drifting gratings is a common method to reveal spatial tuning of cells in the visual system with center-surround organization [67-69]. As yR8 are excited by green, I used a green grating stimuli of varying spatial frequencies. Based on the model, I expected to see surround opponency-evidenced by a peak response at frequencies corresponding to the width of the center, and decreasing responses as bars widened to span more of the surround. The largest amplitude responses in yR8 were measured at a spatial frequency of

10°/cycle, corresponding to bars spanning ~5° (Figure 16C), consistent with the fly's inter-ommatidial angle, or the width of the "center." Stimuli with wider gratings (higher degrees/cycle) elicited a much weaker maximum response in yR8, which is strong preliminary evidence for increasing surround inhibition as multiple ommatidia become stimulated. Thus, this data confirms the existence of a center-surround receptive field organization in photoreceptors, as predicted by our model. The next step in these experiments would be to use a custom-built UV/G/B projector setup to present gratings of different wavelengths, which will test the spectral nature of surround opponency.

Figure 16. Recurrent Model of Color Opponency in R7 and R8 Photoreceptors

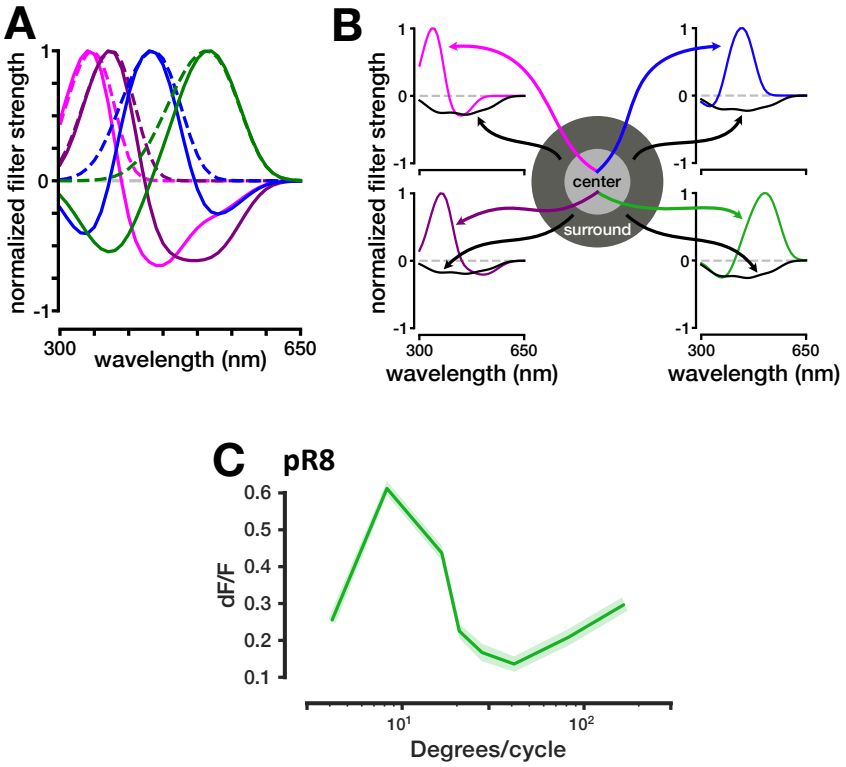

(A) The predicted spectral filtering properties of the different photoreceptor outputs (solid line) compared to the filtering properties of the rhodopsin they express (dashed line). (B) The spectral filtering properties for the predicted center and surround of the different photoreceptor outputs (C) Maximum calcium responses measured in yR8 axons to drifting sine wave gratings of varying spatial frequency (N=6). Peak responsivity corresponds to approximately 10 degrees/cycle.

2.3 Discussion

In this work, I report the spectral tuning of wavelength-specific R7 and R8 photoreceptor outputs in the visual system of the fruit fly *Drosophila melanogaster*. I find that each R7 and R8 output displays distinct spectrally opponent properties. These opponent signals are a consequence of a circuit with dual mechanisms: one that consists of reciprocal inhibition between R7 and R8 from the same ommatidium, enabling UV versus visible comparison at one point in space, and another that supports lateral inhibitory interactions between R7s and R8s from neighboring ommatidia, allowing for additional comparisons to be made in the spectral domain (e.g., blue versus green) between different points in space. I show that the latter is mediated by the horizontal-cell-like Dm9 neuron. A consequence of these dual circuit mechanisms is an efficient decorrelation of photoreceptor signals, which reduces the dimensionality of the system while preserving maximum information.

Spectral Opponency Efficiently Preserves Chromatic Information while Decorrelating Photoreceptor Output Signals

Theories of efficient coding postulate that the purpose of the early visual system is to compress redundant information and remove noise prior to neural transmission [70, 71]. Redundancy stems from correlations that occur extrinsically, in the statistics of natural scenes (chromatically, spatially, and

temporally) but also intrinsically, produced by the strong spectral overlap of the opsin sensitivities of photoreceptors. One well-known way of removing these correlations is via a linear decomposition [24, 70, 71]. In accordance with this, I showed that the photoreceptor outputs of *Drosophila* perform a linear transformation on the inputs that orthogonalizes photoreceptor responses (decorrelation) and creates opposing, near-symmetric chromatic channels (strong anti-correlation). pR7/yR7s and yR8s compare the UV versus the visible part of the spectrum (all crossing over between 380 and 430 nm), forming near-mirror images of each other. pR8s are the only photoreceptors with a three-lobed sensitivity, comparing blue to both UV and green. Using PCA, my colleagues and I found that these axes of opponency efficiently remove correlation in incoming signals resulting from overlapping opsin sensitivities and effectively reduce the dimensionality of the encoding space while maximally preserving spectral information. In other words, the transformation from four photoreceptor channels to two opponent axes allows for a nearly full reconstruction of chromatic information. Achromatic information is likely encoded in neural pathways downstream of R1–R6. However, spectral decorrelation and dimensionality reduction are likely not the only goals, as pR7, yR7, and yR8 photoreceptors all encode spectral inputs along the UV-versus-visible axes. The absolute value of the correlation coefficients of pR7–yR8 and yR7–yR8 outputs is actually larger than the absolute value of their predicted

correlation coefficients at the level of the retina. Such redundancy may serve to deal with noise in the system so that visual stimuli along the UV-versus-visible axis can be robustly encoded [72]. This circuitry could effectively support behaviors that depend on differences between short and long wavelengths.

A Circuit-Constrained Recurrent Model Predicts R7 and R8 Spectrally Opponent Outputs with Complex Spatio-chromatic Receptive Fields

By building an anatomically constrained model of the underlying circuit, my colleagues and I showed that the circuit architecture we identify can quantitatively produce the signals we measured at the level of R7 and R8 outputs. We further constrained our model using synaptic counts obtained from EM. Synaptic count data have been previously used to gain intuition about which inputs to a given neuron are likely strongest [73]. However, it was not clear whether synaptic count could be used more quantitatively to predict function. Using our model, we showed that synaptic count is both a good qualitative and quantitative estimate of synaptic strength. This result demonstrates that, at least in this type of hardwired sensory circuit, synaptic count provides useful in-formation for understanding circuit function.

We used our biologically constrained model to make predictions of the responses of photoreceptor outputs to untested visual stimuli. Our model predicts that the result of this dual opponent system is a spatio-chromatic

receptive field for each photoreceptor output with a UV-versus-visible color opponent center and an antagonistic achromatic surround (Figure 16B). The size of the center is predicted to correspond to one ommatidial angle, or ≤5 degrees [74, 75]. The size of the surround is likely determined by the columnar extent of the horizontal cell Dm9, which has been found to span on average 7 columns [62], corresponding to 35 total degrees in visual space (with a width of ~15 degrees). This prediction was supported by use of spatially patterned green stimuli, which revealed a center-surround organization in pR8 photoreceptors. Moving forward, patterned chromatic visual stimuli with multiple colors will enable direct measurements of receptive field sizes and spectral properties and enable testing of the predictions of our model. Finally, our model does not capture the temporal dynamics of the responses we measure, as we were restricted by the kinetics of our indicator. Further experiments with better time resolution will allow for exploration of both center versus surround and chromatic versus achromatic dynamics—both of which are important features to consider in terms of signal processing and behavioral consequences.

Functional Implications

The Dm9-mediated, inter-ommatidial circuit can be directly compared to mechanisms that establish opponency in the retina of trichromatic primates. There, midget cells compare photon catches between M and L cones, creating a

red-green opponent axis. This opponent channel is thought to be established through non-selective wiring of H1 horizontal cells with M and L cones [17, 76] (but see [77]). In the fovea, each midget ganglion cell receives inputs from a single M or L cone at its center and a mixture of M and L cones in its surround. This so-called "private line" circuitry supports both high acuity and cone opponency, resulting in multiplexed signals capturing both high-resolution achromatic stimuli that isolate the center and low-spatial-resolution chromatic stimuli that engage both center and surround [78, 79]. The ambiguity between these multiplexed signals may be resolved by differential processing at the level of downstream pathways, which may preserve either chromatic signatures at the expense of spatial information or vice versa [80] (but see [26]).

The circuit at the level of photoreceptor outputs is similar to the foveal midget pathway: it is horizontal cell mediated, samples the center at one point in space, samples the surround randomly from the distribution of opsins in the eye, and creates spatially and spectrally opponent responses. Like the midget pathway, R7 and R8 photoreceptor signals also convey multiplexed information, which could be differentially processed downstream. However, a key difference in flies is that the center itself is spectrally opponent, and therefore, signals in the fruit fly would be separated into a high-resolution chromatic pathway and a low-resolution chromatic pathway. A separate high-resolution achromatic pathway also exists in flies, driven by R1–R6, which are active in daylight. Flies

have been shown to discriminate between blue and green large areas of illumination [39, 41], but it remains to be seen whether they take advantage of their capacity for spatially acute color vision behaviorally, as swallowtail butterflies do (Papilio xuthus) [81], but not honeybees (Apis mellifera) [82, 83].

Unlike the simple eye of mammals, the compound eye of the fly is not subject to the limitations of optical aberration. It thus has the capacity to build a chromatic comparison system that operates at the full resolution of the eye, equivalent to the resolution of achromatic pathways. It uses an insect-specific circuit architecture that is well-suited to extract chromatic information for small-target visual stimuli at a scale equivalent to the resolution of the fly eye (~5 degrees). Additionally, the fly uses a horizontal-cell-mediated circuit based on lateral interactions, similar to the one used in primates. This system allows for further chromatic comparisons to be made, like the one I measured between the blue and green parts of the spectrum, and is also well tuned to extract chromatic information for large target visual stimuli. Overall, the dual circuit combines an insect-specific circuit motif, which could enable chromatic vision at the full resolution of the fly eye, and an evolutionarily convergent center-surround circuit motif, which could allow for lower spatial resolution chromatic vision with extended spectral resolution.

2.4 Methods

Key Resources Table

REAGENT or RESOURCE	SOURCE	IDENTIFIER
Antibodies		
sheep anti-GFP	AbD Serotec (BIO-RAD)	#4745-1051, RRID: AB_619712
rat anti-DN-CadN	DSHB	#DN-Ex#8, RRID: AB_528121
mouse anti-Chaoptin	DSHB	#24B10, RRID: AB_528161
rat anti-DYKDDDDK	Novus	#NBP1-06712SS
rabbit anti-beta-galactosidase	MP Bio	#08559762, RRID: AB_2335286
Alexa Fluor 488-conjugated donkey anti-rabbit	Jackson ImmunoResearch	#711-545-152, RRID: AB_2313584
Alexa Fluor 647-conjugated donkey anti-rat	Jackson ImmunoResearch	#712-605-153, RRID: AB_2340694
CY3-conjugated donkey anti-rat	Jackson ImmunoResearch	#712-165-153, RRID: AB_2340667
Alexa Fluor 647-conjugated donkey anti-mouse	Jackson ImmunoResearch	#715-605-151, RRID: AB_2340863
Alexa Fluor 488-conjugated donkey anti-sheep	Jackson ImmunoResearch	#713-545-147, RRID: AB_2340745
Alexa Fluor 555-conjugated donkey anti-mouse	Thermo Fisher Scientific	#A31570, RRID: AB_2536180
Experimental Models: Organisms/Strains		
D. Melanogaster: Rh3-Gal4	Desplan Lab, NYU (Cook et al., 2003)	N/A
D. Melanogaster: Rh6-Gal4	Desplan Lab, NYU (Cook et al., 2003)	N/A
D. Melanogaster: Rh4-Gal4	Desplan Lab, NYU (Saint-Charles et al., 2016)	N/A
D. Melanogaster: Rh5-Gal4	Desplan Lab, NYU (Saint-Charles et al., 2016)	N/A
D. Melanogaster: 20X-UAS-GCamp6f; PBac(20XUAS-IVS-GCaMP6f)VK00005	Bloomington Drosophila Stock Center	BDSC: 52869 FlyBase: FBti0156888

D. Melanogaster: R21A12-Gal4; P(GMR21A12-GAL4)attP2	Bloomington Drosophila Stock Center	BDSC: 48925 FlyBase: FBti0133834
D. Melanogaster: R32E04-Gal4; P(GMR32E04-GAL4)attP2	Bloomington Drosophila Stock Center	BDSC: 49717 FlyBase: FBti0134886
D. Melanogaster: UAS-Kir2.1	Axel Lab, Columbia	N/A
D. Melanogaster: Rh5-LexA	Desplan Lab, NYU (Vasiliauskas et al., 2011)	N/A
D. Melanogaster: UAS-NorpA1	Wernet Lab, Free University of Berlin (Wernet et al., 2012)	N/A
D. Melanogaster: UAS-NorpA2	Gift from Matthias Wernet (Wernet et al., 2012)	N/A
D. Melanogaster: $hiscl^{134}$ ort^{1}	Wernet Lab, Free University of Berlin	N/A
D. Melanogaster: $hiscl^{134}$ ort^{1} cry^{02}	Rouyer Lab, Paris-Saclay Institute of Neuroscience (Alejevski et al., 2019)	N/A
D. Melanogaster: UAS-Ort	Rouyer Lab, Paris-Saclay Institute of Neuroscience (Alejevski et al., 2019)	N/A
D. Melanogaster: UAS-mCD8; P(UAS-mCD8::GFP.L)LL6	Bloomington Drosophila Stock Center	BDSC: 5130 FlyBase: FBti0012686
D. Melanogaster: hs-FLPG5.PEST and 10XUAS(FRT)myr::smGdP-705V5/FLAG/HA-10XUAS(FRT); P(hs-FLPG5.PEST)attP3, P(10xUAS(FRT.stop)myr::smGdP-V5-THS-10xUAS(FRT.stop)myr::smGdP-FLAG)su(Hw)attP1, PBac(10xUAS(FRT.stop)myr::smGdP-HA)VK00005	Bloomington Drosophila Stock Center	BDSC: 64085 FlyBase: FBti0169301, FBti0169283, FBti0169255
D. Melanogaster: Rh4-LacZ	Desplan Lab, NYU	N/A
Oligonucleotides		
Primer: Ort Forward: CAAAGTCTGGCCATAACCGAC	Hong et al., 2006, IDT	N/A
Primer: Ort Reverse: AACAGGTGGCAAAGACGACTG	Hong et al., 2006, IDT	N/A
Primer: HisCl Forward: ATTGTAGAGCACGTATTTGC	Hong et al., 2006, IDT	N/A

Primer: HisCl Reverse: TCCATCATAGGAACGTTGTC	Hong et al., 2006, IDT	N/A
Primer: Gal4 Forward: AAGTGCGACATCATCATCGGAA	Barret et al., 2008, IDT	N/A
Primer: Gal4 Reverse: CAGTTCTTTGTGCTGCATCGCT	Barret et al., 2008, IDT	N/A
Primer: UAS Forward: AAGCGAAAGCTAAGCAAATAAAC	This paper, IDT	N/A
Primer: UAS Reverse: TAGCAATTCTGAAGGAAAGTC	This paper, IDT	N/A
Primer: LexA Forward: AAACGCGGCTGAAGAACATCTG	This paper, IDT	N/A
Primer: LexA Reverse: TTTCTGGCAACAGTTCGACTTTATTGC	This paper, IDT	N/A
Primer: GCaMP Forward: GTTGCCGTCGTCCTTGAAGAAG	This paper, IDT	N/A
Primer: GCaMP Reverse: GCCTACCACTACCAGCAGAACA	This paper, IDT	N/A
Software and Algorithms		
Python 3.6	Python Software Foundation	https://www.python.org
SciPy	SciPy	https://github.com/scipy/scipy
Lmfit	LMfit	https://github.com/lmfit/lmfit-py/
CaImAn	Flatiron Institute; Giovannucci et al. 2019	https://github.com/flatironinstitute/CaImAn
Analysis and Modeling Code	This paper	N/A
Calcium signal extraction code	This paper	https://gitlab.com/rbehnialab/colorvisionpaper1
Stimulus Software	This paper	https://gitlab.com/rbehnialab/motyxia2
Fiji	NIH	https://fiji.sc/
ImageJ	NIH	https://imagej.net/mbf
DataJoint	Datajoint; Yatsenko et al, 2018	https://github.com/gucky92/datajoint-python (fork from main project)
OpenCV	opencv	https://opencv.org
Sklearn	Scikit-learn	https://scikit-learn.org

Experimental Model and Subject Details

w+ flies were reared on standard molasses-based medium at 25C - 28C. The rhodopsin drivers used for imaging photoreceptors Rh3-Gal4 and Rh6-Gal [84] along with Rh1-Gal4, Rh4-Gal4 and Rh5-Gal4 [85] were expressed heterozygously along with 20X-UAS- GCaMP6f, also expressed heterozygously (Bloomington stock center: 52869). Dm9 cells were targeted for imaging, staining and silencing using both the R21A12-Gal4 or the R32E04-Gal4 drivers (Bloomington stock center: 48925 and 49717). Silencing was per- formed using UAS-Kir2.1 constructs (made and gifted by by Daisuke Hattori), and imaging with Rh5-LexA [86] (gift from Claude Desplan) and LexAop-GCaMP6f (BL44277). Phototransduction rescue experiments were performed using *norpa*- and UAS-NorpA1 or UAS-NorpA2 constructs [53] (gifts from Mathias Wernet). Ort rescue experiments were performed in a $hiscl^{134}ort^{1}$ background (gift from Mathias Wernet), heterozygous with $hiscl^{134}ort^{1}cry^{02}$ [87] by also expressing a UAS-ort construct [87] (both gifts from Francois Rouyer). For immunostaining, UAS-mCD8 (gift from Claude Desplan) or UAS-GCaMP6f (Bloomington stock center: BL42747) constructs were used to label cell types of interest. For clones, hs-FLPG5.PEST and 10XUAS(FRT)myr::smGdP-V5/FLAG/HA-10XUAS(FRT) constructs were used (Bloomington Stock center 64085) as well as Rh4-LacZ [88] (Gift from Claude Desplan). For optogenetic imaging, Dm9 cells were targeted with the R32E04-LexA driver (Bloomington stock center:

BL54739), and the 13X-LexAop2-IVS-Syn21-Chrimson-tdTomato-3.1 construct (gifted by Barret Pfeiffer, Allan Wong and David Anderson). R7 photoreceptors were simultaneously imaged using a panR7-Gal4 driver (gift from Claude Desplan). Control flies expressed both panR7-Gal4 and UAS-GCaMP6f constructs, but were missing either the R32E04-LexA driver or the 13X-LexAop2-IVS-Syn21-Chrimson-tdTomato-3.1 construct. All flies for optogenetic imaging were *norpa*- mutants.

Two-Photon Calcium Imaging

Imaging was conducted with a two-photon microscope (Bruker) controlled by PrairieView 5.4 and a mode-locked, dispersion compensated laser (Spectraphysics) tuned to 930 nm. We imaged with a 20x water-immersion objective (Olympus XLUMPLFLN, 1.0 numerical aperture). In front of the photomultiplier tube (Hamamatsu GaAsP), we mounted a band-pass filter (Semrock 514/ 30 nm BrightLine) to reduce bleed-through from the visual stimulus setup. T-Series were acquired at 15-30Hz and lasted for a maximum of eight minutes with each frame at x-y imaging being 145x90 pixels.

All experimental animals for functional imaging were briefly anaesthetized using carbon dioxide on the day of eclosion, and imaged at ages ranging from 3-13 days. Flies were prepared for two-photon imaging based on methods previously described [89]. Flies were anesthetized using ice, and mounted in a

custom stainless-steel/3D-printed holder. A window was cut in the cuticle on the caudal side of the head to expose the medulla, where the axons of photoreceptors could be imaged. The eyes of the of the fly remained face down under the holder, and remained dry while viewing the visual stimuli, while the upper part of the preparation was covered with saline. The saline composition was as follows (in mM): 103 NaCl, 3 KCl, 5 n-*tri(hydroxymethyl)-methyl-1Aminoethane-sulphonic acid*, 8 trehalose, 10 glucose, 26 NaHCO3, 1 NaH2PO4, 1.5 CaCl2, and 4 MgCl2, adjusted to 270mOsm. The pH of the saline was equilibrated near 7.3 when bubbled with 95% O2 / 5% CO2 and perfused continuously over the preparation at 2 ml=min. The imaging region of interest was limited to the region of the medulla photoreceptors are directly activated by stimuli. Specifically, the z-depth was zeroed at the same level for each fly (the dorsal part of the medulla) and photoreceptor responses were measured from 50-90 microns below that point. Responses were measured from the rostral fourth of the medulla in that plane. The dorsal third of the eye was covered with black acrylic paint to avoid the region where Rh3 and Rh4 are coexpressed in R7s [90]. Calcium responses were stable throughout imaging.

Flies used in optogenetic experiments were reared in the dark on fly food supplemented with all trans-Retinal (1mM, Sigma-Aldrich #R2500). 7-8 day old flies were imaged under the two-photon microscope in the in vivo preparation configuration described previously. Light activation of the Chrimson ion channel

was achieved with a 660nm LED (Thorlabs M660L4) fit with a long pass filter (Thor- labs, 10LWF-400-B). The LED was mounted directly above the preparation and delivered at 33Hz light pulses of 0.195 mW/(mm2) irradiance for a duration of 1 s. Image acquisition was continuous during light activation. Light pulses were repeated 10 times with 30 s intervals between. The expression of the Dm9 driver was verified after each imaging session by viewing td-Tomato excited at 1020nm.

Immunohistochemistry

Immunostainings were done as described by Morante and Desplan [91] with some modifications. Adult flies were anesthetized on ice. Brains were dissected in PBS and fixed in 4% formaldehyde for 35 minutes on ice. Brains were incubated at 4C overnight with the following primary antibodies: sheep anti-GFP (1:500, AbD Serotec), rat anti-DN-cadherin (1:50, DSHB) and mouse anti-chaoptin (1:50, DSHB) diluted in PBST (0.3% Triton X-100 in PBS). Secondary antibodies were incubated for 2 hours at room temperature. Images were acquired using a Nikon A1R Confocal Microscope.

To obtain Dm9 clones, 2-3 day old flies were heat shocked for 3 minutes at 39C and dissected 2 days later. Dm9 clones were labeled with the FLAG epitope tag using the primary antibody rat anti-DYKDDDDK (1:200, NBP1). Yellow R7

photoreceptors were labeled with an Rh4-LacZ reporter construct and the primary antibody rabbit anti-beta-galactosidase (1:2000, MBP).

Visual Stimulation Hardware

We produced full-field wavelength-specific stimuli using a customized setup (Figure 1.1C). The setup consists of six LEDs in the UV and visible wavelength range (ThorLabs M340L4 - dUV/340nm; M365L2 - UV/360nm; M415L4 - violet/415nm; M455L3 - blue/455nm; M565L3 - lime/565nm; M617L3 - orange/615nm). A customized driver drove the five LEDs from dUV to lime. These LEDs turned on during the return period of the x-scanning mirror in the two-photon microscope (fly-back stimulation). We used the TTL signal generated by the two-photon microscope at the beginning of each line-scan of the horizontal scanning mirror (x-mirror) to trigger the LED driver. An individual T-Cube (Thorlabs LEDD1B T-Cube) drove the orange LED. Stimuli were generated using customized software written in Python. The update rate for the LED voltage values was 180Hz.

The different light sources were focused with an aspheric condenser lens (ThorLabs ACL2520U-A) and aligned using dichroic mirrors (dUV-UV dichroic - Semrock LPD01-355RU; UV-violet dichroic - Semrock FF414-Di01; violet-blue dichroic - Semrock Di02-R442; blue-lime dichroic - Semrock FF495-Di03; lime-orange dichroic - Semrock FF605-Di02). The collimated light passed through a

diffuser (ThorLabs DG10-1500A) before reaching the eye of the fly, which is positioned 2cm away.

Intensity Calibration

In order to measure the intensity of our LEDs across many voltage outputs, we used a photo-spectrometer (250-1000 nm, Ocean Optics) that was coupled to an optic fiber and a cosine corrector and was controlled using our customized Python software. The photo-spectrometer was mounted on a 3D printed holder that was designed to fit on our experimental rig and approximately aligned with the fly's point of view. For each LED, we tested a total of 40 voltage values (linearly separated) from the minimum voltage output to the maximum voltage output. For each voltage value tested, we adjusted the integration time to fit the LED intensity measured, and averaged over 20 reads to remove shot noise.
Using the spectrometer output, we calculated the absolute irradiance ($I_p(\lambda)$; in W=m^2mI across wavelengths using the following equation:

$$I_p(\lambda) = C_p(\lambda)\frac{S_p(\lambda) - D_p(\lambda)}{\Delta t \cdot A \cdot 100} \qquad \text{(Equation 1)}$$

where $C_p(\lambda)$ is the calibration data provided by Ocean Optics ($\mu J/count$), $S_p(\lambda)$ is the sample spectrum (counts), $D_p(\lambda)$ is the dark spectrum $(counts)$, Δt is the integration time (s), and A is the collection area (cm^2).

Next, we converted absolute irradiance to photon flux (E_q; $in\ \mu E/nm$):

$$E_p(\lambda) = \frac{I_p(\lambda) \cdot c \cdot \lambda}{h \cdot N_A \cdot 10^6} \quad \text{(Equation 2)}$$

where $h \bullet c / \lambda$ is the energy of a photon with h as Planck's constant ($6.63 \bullet 10^{-34} \bullet J \bullet s$), c as the speed of light ($2.998 \bullet 10^8$ m/s), and λ the wavelength (nm). N_A is Avogadro's number ($6.022 \bullet 10^{23}$ mol^{-1}).

Stimulus Design

Each stimulation protocol had 10–20 s before and after the stimulation period in order to measure baseline fluorescence (fluorescence to background light). Because we anticipated measuring opponent waveforms at the level of photoreceptor outputs, we used single wavelength dominant backgrounds (UV for R7s and blue for R8s), which have the advantage of highlighting opponent signals. In these conditions, GCaMP6f fluorescence was increased at baseline, allowing decreases to be readily measured.

For the correlation analysis, PCA, and modeling, we acquired an additional dataset of spectral tuning measurements, in which measurements for all photoreceptor types were made with the same stimulus over a large range of intensities and combinations of single wavelengths. We used a background with a flat spectrum at an intensity of 10mE with luminant multiples ranging over several orders of magnitude. The opponent waveforms we measure under these

conditions are consistent with our wavelength-dominant background experiments. For Dm9 recordings, we also used the flat spectrum.

The intensities of each LED for the different background conditions are shown in Table 1:

Table 1. Background light intensities.

LED	UV-dominant	Blue-dominant	South-dominant
dUV	$<10^{-4}$	$<10^{-4}$	1.08
UV	1.0	$<10^{-4}$	1.35
Violet	$<10^{-4}$	$<10^{-4}$	1.69
Blue	$<10^{-4}$	0.2	1.40
Lime	$<10^{-4}$	$<10^{-4}$	2.61
Orange	$<10^{-4}$	$<10^{-4}$	1.88

Flies were adapted to the different background lights for approximately 5 minutes before the start of the recording. For the flat background condition, we chose the intensities of the LEDs by fitting the following equation:

$$\min\left\{\|\mathbf{Lx}-\mathbf{b}\|^2,\ \mathbf{l}\le\mathbf{x}\le\mathbf{u}\right\} \qquad \text{(Equation 3)}$$

where L is a matrix of the normalized LED intensities across wavelengths (each row is a different wavelength and each column is a different LED), x is a vector of corresponding LED intensities to fit, and b is the background spectrum across wavelengths (i.e., a flat spectrum with an overall intensity of 10 μE). x is bounded by the minimum l and maximum u intensity each LED can reach. The

minimum intensity is zero for all LEDs, and the maximum intensities are (in μE): dUV – 11.7, UV – 21.7, violet – 17.0, blue – 16.4, lime – 18.7, and orange – 145.1.

We wanted to show different single Gaussian wavelengths between 320–620 nm with a standard deviation of 10 nm on top of our background (i.e., add these single wavelengths to our background light) (Figure 1.1F). We also wanted to show these single wavelengths across different intensities. To do this, we built a simple model of opsin photon capture.

The absolute photon capture of an opsin (i.e., the number of photons absorbed) given any spectral stimulus at a specific intensity can be calculated as follows [54, 55]:

$$Q_i = C_i \int S_i(\lambda) I(\lambda) d\lambda \qquad \text{(Equation 4)}$$

where Q_i is the absolute photon capture of opsin i, C_i is the absolute sensitivity of opsin i, S_i is the relative spectral sensitivity of opsin i, and I is the spectrum of light entering the eye. Equation 4 implies that the identity of a photon is lost upon absorption by a photoreceptor (i.e., the principle of univariance). As the scaling factor C_i is usually unknown, the relative photon capture can be calculated instead assuming von Kries chromatic adaptation [55, 92, 93]:

$$q_i = \frac{Q_i}{Q_i^b} \qquad \text{(Equation 5)}$$

where q_i is the relative photon capture of opsin i, and Q^b_i is the absolute photon capture of opsin i for the background illuminant.

For our six LEDs, we can calculate the normalized relative capture across the fly opsins:

$$\mathbf{A} = \mathbf{SL} \oslash \mathbf{p} \qquad \text{(Equation 6)}$$

where $\mathbf{A}$ is a matrix corresponding to the relative photon capture of each opsin for each LED *(opsin x LED)*, $\mathbf{S}$ is a matrix of the relative spectral sensitivities for all opsins across wavelengths *(opsin x wavelength)*, $\mathbf{L}$ is a matrix of the normalized LED intensities across wavelengths *(wavelength x LED),* and $\mathbf{p}$ is a vector of the absolute capture for all opsins for the background spectrum. $\oslash$ signifies element-wise division.

To emulate our desired stimuli using our six LEDs, we first calculate the relative photon capture of each opsin present in the fly eye given the desired stimulus. This gives us a vector $\mathbf{q}$. Given $\mathbf{A}$ from Equation 6, we find the optimal intensities for each LED to match our desired $\mathbf{q}$ as follows:

$$\min\left\{\|\mathbf{w} \odot (f(\mathbf{Ax}) - f(\mathbf{q}))\|^2,\ \mathbf{l} \le \mathbf{x} \le \mathbf{u}\right\} \qquad \text{(Equation 7)}$$

where $\mathbf{x}$ is a vector of corresponding LED intensities to fit, w is a weighting factor for each opsin, and f is a link function (i.e., the identity for the single wavelength dominant backgrounds and the log for the flat background). The weighting factor w was 1 for all opsins in the case of the single wavelength

dominant backgrounds, and 1 for all opsins, except 0.1 for Rh1, in the case of the flat background. The lower ($\mathbf{l}$) bound on $\mathbf{x}$ corresponds to the background intensity of each LED, as we desired to add a spectrum on top of the background. The upper ($\mathbf{u}$) bound on $\mathbf{x}$ correspond to the maximum intensity each LED can reach. $\odot$ signifies element-wise multiplication.

We used a total of three stimulus sets. The accuracy of our fitting procedure is shown in Figures 2G–2R. Each individual stimulus (i.e., each simulated wavelength or wavelength mixture) lasted 0.5 s with a 1.5 s period between stimuli. The background intensity values are shown in Table 1. Our UV-dominant and blue-dominant background was used to test the existence of color opponency in R7s and R8s, respectively. Both stimulus sets had a total of 16 wavelengths that were tested spanning 320 to 620 nm, and each stimulus was repeated three times. In the case of the UV-dominant background, each wavelength was fitted using an intensity that was 5 times bigger than the total background intensity (i.e., a luminant multiple of 5). In the case of the blue-dominant background, the wavelengths were a luminant multiple of 15. In the case of the UV-dominant background, we discarded the simulated wavelengths 480, 500, and 520 nm, because the dUV LED is on for these longer fitted simulated wavelengths; the algorithm was trying to fit the relative capture of the broadband rh1 opsin (Figures 2A, 2G, and 2M). In the case of the blue-dominant background, we discarded the wavelengths 360 and 440 nm, because the green

and orange LED is on respectively for these shorter fitted simulated wavelengths; the algorithm was trying to fit the relative capture of the broadband Rh1 opsin (Figures 2B, 2H, and 2N). To avoid this issue during fitting of the flat background stimuli, the error for the Rh1 capture is weighted differently (Equation 7). This is reasonable considering R1–6 photoreceptors do not contribute significantly to R7 and R8 photoreceptor responses (Figures 1.6I–1.6P).

For the flat background our single wavelengths included: 320 nm, 340 nm, 360 nm, 380 nm, 400 nm, 420 nm, 440 nm, 460 nm, 500 nm, 530 nm, 570 nm, 620 nm. We tested luminant multiples of 0.2, 1, 4, and 8. We also mixed the wavelengths 340 nm and 440 nm, 380 nm and 620 nm, 320 nm and 530 nm, 460 nm and 570 nm, and 400 nm and 570 nm. As predicted, putative rhabdomeric responses correspond to the log of the relative photon capture (Figures 3B–3E), we mixed wavelengths in the following way to test for linearity:

$$\log(\mathbf{q}_{mix}) = p\log(\mathbf{q}_{w/1}) + (1-p)\log(\mathbf{q}_{w/2})$$
$$\mathbf{q}_{mix} = \mathbf{q}_{w/1}^{p} \cdot \mathbf{q}_{w/2}^{1-p} \qquad \text{(Equation 8)}$$

where $\mathbf{q}_{\mathrm{mix}}$ is the calculated relative capture for the mixture of wavelengths, p is the proportion of wavelength $w/1$, $\mathbf{q}_{\mathrm{w}}/1$ is the calculated capture of wavelength $w/1$, and $\mathbf{q}_{\mathrm{w}}/2$ is the calculated capture of wavelength $w/2$. Using Equation 7, we fit the calculated captures for the mixture of wavelengths, as we did for the

single wavelengths. For testing linearity of our responses, we used the mixtures at the luminant multiple of 1, as it provided good fits in our regression (see Figures 2D, 2J, 2P, and 2S–2W) and large calcium responses (see Figures 1.10).

For any analysis work we used the calculated relative capture after fitting and not the target relative capture we were aiming to simulate.

Quantification of Imaging Data

All data analysis for in vivo calcium imaging was performed in Python using custom-made Python code and publicly available libraries. To correct our calcium movies for motion we performed rigid translations based on template alignment using the algorithm provided by the CaImAn package [94]. As a template for rigid motion correction, we used the average projection of the first ten seconds of every calcium movie during which we did not show any visual stimuli.

Region of interests (ROIs) were selected automatically using a custom-made approach and verified manually. A standard deviation projection was taken of the complete image stack. We thresholded the projected image in three ways to identify pixels that are certainly part of a ROI, certainly part of the background, and possibly part of a ROI. These thresholded images were used to identify connected components (i.e., individual ROIs). Next, we applied a

watershed transformation to obtain the individual ROIs. We discarded any ROIs of fewer than 5 pixels.

To extract calcium traces from our segmented images, we first took the average fluorescence of each ROI at each time point. We subtracted the mean background fluorescence – the mean fluorescence of all pixels that do not belong to any ROI – from each trace to remove background noise. To calculate the dF/F signal, we used as a baseline for our denoised traces the 5th percentile of a rolling 30 s time window. Finally, we smoothed our dF/F signal with a Gaussian filter of size 0.32 s and a standard deviation of 0.08 s. We discarded ROIs, where the signal-to-noise *(SNR)* ratio was smaller than 1.5. The *SNR* was defined as the standard deviation of the signal during stimulation over the standard deviation of the signal before and after the start of stimulation ($SNR = \sigma_{stim} = \sigma_{baseline}$).

dF/F traces were aligned to the stimulus start times and averaged for each ROI. Amplitude measurements were taken on these aver- aged PSTHs for each ROI. As each stimulus was 0.5 s long amplitudes were calculated by taking the average dF/F response between 0.42 and 0.5 s after the stimulus onset and subtracting the average dF/F response 0.15 to 0.05 s before stimulus onset (i.e., the base- line). The max-dF/F signal of the spectral tuning curves was calculated by dividing the mean across all ROIs of the wavelength with the maximum response.

In the case of the double NorpA rescues, we needed to sort our individual ROIs. To do this, we fitted the data to the log of the relative photon capture of the opsin each photoreceptor expresses. For example, in the case of the pR8 and yR8 NorpA rescues, we fitted each ROI to the log of the relative photon capture of Rh5 and Rh6 separately. Next, we assigned each ROI to the cell type according to which fit explained more of the variance. In our example, if the Rh5 fit is better than the Rh6 fit for a ROI, that ROI is a putative pR8 axon.

Correlation and Principal Component Analysis

To calculate the correlation coefficients of actual and predicted responses, we first calculated the covariance matrix ($\mathbf{\Sigma}$). We calculated the covariance as follows:

$$\mathbf{\Sigma} = \mathbf{Y}^T\mathbf{Y} \qquad \text{(Equation 9)}$$

where $\mathbf{Y}$ are the responses of the different cell types across stimuli (*stimulusxcell-type*).

We calculate the correlation coefficient matrix ($\mathbf{C}$), as follows:

$$\mathbf{C} = \frac{\mathbf{\Sigma}}{\sqrt{diag(\mathbf{\Sigma})diag(\mathbf{\Sigma})^T}} \qquad \text{(Equation 10)}$$

To obtain principal components of our retinal inputs, we first calculated the covariance matrix ($\mathbf{\Sigma}$). In the case of a uniform Fourier frequency power

spectrum (flat stimulus spectrum), we calculated the covariance using the spectral sensitivities of each opsin, similar to Buchsbaum and Gottschalk [24]. We used the log-plus-one transformed spectral sensitivity for our covariance calculation to account for our observation that the retinal response is proportional to the log of the relative photon capture. This log-plus-one transformation had a negligible effect on the actual principal components obtained. In the case of the hyperspectral reflectance dataset, we first calculated the relative photon capture of each opsin for each reflectance and applied a log transformation. The covariance was calculated on this dataset as in Equation 9.

In order to decompose the opsin spectral sensitivities, we simply eigendecompose the covariance S to obtain eigenvalues and eigenvectors. This is equivalent to principal component analysis (PCA), where the eigenvectors correspond to the different components and the eigenvalues are proportional to the explained variance for each component. To construct principal component tuning curves, we took the dot product of the photoreceptor inputs (*stimulus xopsin*) and the eigenvectors (*opsinxcomponent*).

We also compared our complete principal component analysis of the hyperspectral dataset to the decomposition of inputs along a segregated pale and yellow columnar organization[38], corresponding to intra-ommatidial interactions alone; i.e., performing PCA on the pale and yellow inputs separately

(Figure 14D). The two chromatic components obtained this way are, somewhat trivially, still correlated, as only retinal inputs from the same type of ommatidium are decomposed (Figures 12E and 12F). Due to the large overlap of the spectral sensitivities between pale and yellow photoreceptors, these two separate chromatic components have a correlation coefficient of 0.6. This indicates that having two separate chromatic pathways (that just rely on intra-ommatidial connections) creates an inefficient representation of the color space available to the fly. Instead, the circuit we describe, combining both intra- and inter-ommatidial interactions, displays more complete opponent mechanisms at the early photoreceptor level than previously thought, and is also capable of efficient encoding and transmission of chromatic information.

We obtained the hyperspectral reflectance dataset from http://www.reflectance.co.uk [95-99]. The obtained hyperspectral reflectances and the opsin sensitivities were linearly interpolated between 300 and 600nm to calculate the relative photon capture. The dataset mostly contains a variety of flower reflectances. While flowers are not known to be of relevance in Drosophila ecology, we argue that in general, natural reflectances in defined wavelength ranges are very similar, and thus comparable for purposes of decomposition [100].

Linearity of the System

We asked if photoreceptor axonal outputs are linear with regard to their calculated rhabdomeric inputs (i.e., log(q)). For this analysis, we acquired an additional dataset of spectral tuning measurements, in which measurements for all photoreceptor types were made with the same stimulus over a large range of intensities(Figure 12). We used a background with a flat spectrum at an intensity of 10 μE with luminant multiples ranging over several orders of magnitude (Figure 3). The opponent waveforms we measure under these conditions are consistent with our previous experiments. To test for linearity, we assessed two empirical measures: scalar invariance and additivity. The estimated zero-crossing points of the opponent tuning curves of R7s/R8s do not significantly change at different intensities of light measurements, showing scalar invariance within the bounds of our recording conditions. To test for additivity, we measured the responses of photoreceptor outputs to wavelengths mixed in different ratios (see Equation 8) and compared the responses to corresponding linear additions of the single wavelength responses. The measured responses to the mixtures (filled circles) do not significantly differ from the linear predictions (shaded area). Therefore, the circuit under investigation behaves linearly within the range of stimuli used in this study.

Linear Regression

To assess chromatic tuning of our responses, we fit a linear regression model to our data:

$$\mathbf{r} = \mathbf{X}\beta \quad \text{(Equation 11)}$$

where $\mathbf{r}$ is the average amplitude response of a neuron type to the various stimuli in the flat background condition, $\mathbf{X}$ is the input space (i.e., the $\log q$ for each stimulus), and β is the vector of the associated weights for each input feature. Fitting was performed using 4- fold cross-validation. To improve numerical stability during the fitting procedure without biasing the end result, fitting was performed on a ‘‘whitened’’ input space (PCA whitening). After fitting, parameters were transformed back into ‘‘unwhitened’’ space. In order to assess goodness of fit for the different inputs, we calculated the 4-fold cross-validated R2 values for each input space.

Circuit Modeling

Given the hypothesized circuit architecture, we built a linear recurrent model described by the following equations:

$$\tau_r \frac{d\mathbf{r}}{dt} = -\mathbf{r} - \mathbf{W}\mathbf{r} + \mathbf{y}_e e + \log(\mathbf{q}) \quad \text{(Equation 12)}$$

$$\tau_e \frac{de}{dt} = -e - \mathbf{y}_i^T \mathbf{r} \quad \text{(Equation 13)}$$

where $\mathbf{r}$ is a vector of the responses of the photoreceptor axons, $\mathbf{W}$ is the connectivity matrix for the direct inhibitory connections, t is the time constant, $\mathbf{y_e}$ is a vector of the synaptic weight from Dm9 back to each photoreceptor, $\mathbf{e}$ is

the response of Dm9, $\mathbf{q}$ is the relative photon capture, $\mathbf{y_i}$ is the synaptic weights from the photoreceptors to Dm9. All weights are positive, and the inhibitory or excitatory nature of the synapse is indicated by the sign.

We can simplify the above equation by setting de/dt = 0, dr/dt = 0 (i.e., steady-state condition), so that:

$$(\mathbf{I} + \mathbf{W} + \mathbf{y_e}\mathbf{y_i}^T) \cdot \mathbf{r} = \log(\mathbf{q}) \quad \text{(Equation 14)}$$

where $\mathbf{I}$ is the identity matrix. Using Equation 14, we fit the model to all our flat background data using least-squares and cross-validated our fits 4-fold. To normalize synaptic counts [58, 60, 61], we divided the synaptic count by the total number of synapses for each neuron. To change the gains of individual neurons using these fixed weights, we fit the Dm9 gain c and the photoreceptor gains a in the following equation using least-squares:

$$(\mathbf{I} + \mathbf{W} + c \cdot \mathbf{y_e}\mathbf{y_i}^T) \cdot (\mathbf{a} \odot \mathbf{r}) = \log(\mathbf{q}) \quad \text{(Equation 15)}$$

We used our synaptic count + gain model fits for our prediction of the spectral filtering curve and center-surround receptive field. The spectral filtering curve is the predicted response to individual narrow single wavelengths (instead of broader single wavelengths which we were able to test). The center-surround receptive field was normalized to each peak response. The center corresponds to the predicted response, when removing the Dm9 interneuron (center = $(\mathbf{I} + \mathbf{W}) \cdot (\mathbf{a} \odot \mathbf{r})$). The surround corresponds to the response to the input of each photoreceptor receives from Dm9 (surround = $c \cdot \mathbf{y_e}\mathbf{y_i}^T \cdot (\mathbf{a} \odot \mathbf{r})$).

Quantification and Statistical Analysis

The statistical details of each experiment can be found in the Figure legends. For all PSTHs and tuning curves, we show the empirically-bootstrapped 95% confidence interval to indicate significance. To obtain these intervals, we randomly resampled from our data (independently across all ROIs) 1000 times and recalculated the mean. Next, we took the 2.5% and 97.5% percentile of our 1000 samples.

Data and Code Availability

We used common scientific Python packages for data management, analysis and modeling work, including numpy, scipy, matplotlib, sklearn, DataJoint [101], opencv, and, lmfit. Custom code related to calcium signal extraction is accessible on GitLab (https://gitlab.com/rbehnialab/colorvisionpaper1). The source code used for visual stimulation is available on GitLab (https://gitlab.com/rbehnialab/motyxia2). Raw data supporting the current study have not been deposited in a public repository because of their large size, but are available from the Lead Contact, Rudy Behnia (rb3161@columbia.edu).

Contributions to Chapter 2

I want to thank my mentor Rudy Behnia, and my labmate Matthias Christenson for cowriting many sections of this text with me (see [65]). I really want to emphasize the role of Matthias, who processed and analyzed the imaging data, wrote the visual stimulation code, and performed the modeling work.

Chapter 3: *Drosophila* Opsin Sensitivity Depends on Adaptation State

3.1 Introduction

Recently, there has been renewed interest in *Drosophila melanogaster* as a genetically tractable system to study circuit level mechanisms of color vision [38-43]. Indeed, the fruit fly is equipped with four cone-like photoreceptors which express different opsins (Figure 17 A-D, see also Chapter 1). The dark-adapted sensitivities of the narrow-band opsins expressed in these photoreceptors have recently been measured *in vivo* [102] (Figure 17C).

In most cases, including the most recent study in *Drosophila,* spectral sensitivities of model organisms are measured in the dark-adapted state[103-108]. However, it has been shown in a variety of species, including insects, that spectral sensitivity measurements in both photoreceptors and downstream cells can vary greatly in a dark- versus light-adapted state[109-111]. In moths, this has been shown to be due to a "pupil" mechanism in which pigment granules in rhabdomeres migrate to the surface in a light-adapted state, thus absorbing additional photons and reducing sensitivity [111]. *Drosophila* have been shown to have this same psuedopupil mechanism [112], and thus are likely to experience opsin sensitivity shifts in different lighting conditions. Light-adapted *Drosophila* opsin sensitivities have not been measured, and thus the dark-

adapted spectral sensitivities previously measured in the fruit fly may not provide a holistic picture of inputs to color vision circuits[49, 102].

Here, I measure rhabdomeric responses in *Drosophila* adapted to darkness, a dawn-like spectrum, and a morning-like spectrum (Figure 17F). I also measure responses at the photoreceptor output level in R7s and R8s in flies adapted to these different backgrounds. Together, these experiments allow me to test for differences due to adaptation state at two separate levels in the visual system of the fruit fly.

Figure 17. Experimental Setup and Stimulus Design

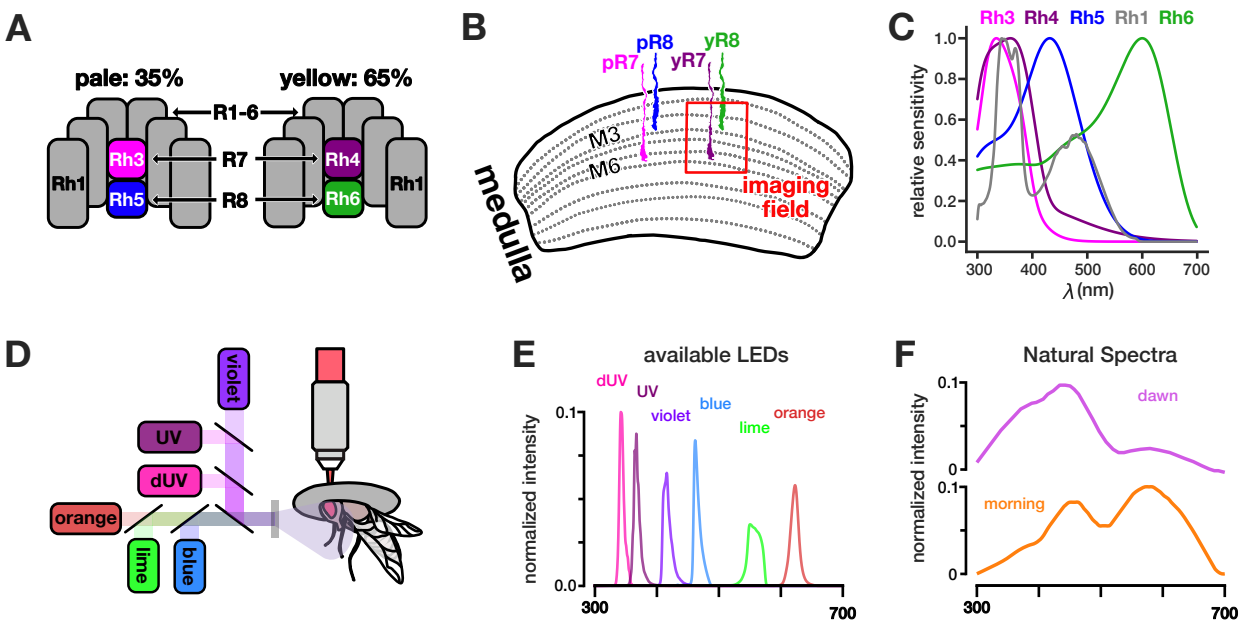

(A) Spectral composition of pale and yellow ommatidia of the Drosophila eye. Pale ommatidia express Rh3 and Rh5 in R7 and R8, respectively. Yellow ommatidia express Rh4 and Rh6 in R7 and R8, respectively. R1–R6 all express Rh1. (B) Photoreceptors in Drosophila project from the retina into the optic lobe. My imaging experiments target the axon terminals of R7 and R8 in the medulla at the level of layers M6 and M3, respectively. (C) Relative spectral sensitivity of opsins expressed in the fruit fly retina; data from [102] and fitted with equation from [50]. (D) Two-photon imaging setup. The fly is secured facing LED setup, and LED sources are combined using a custom color mixer to form a single collimated beam. (E) Normalized photon flux across the wavelength spectrum, corresponding to the various LEDs used for stimuli. (F) Natural spectra obtained from (ref). Flies are adapted to either of these spectra or complete darkness for 3–5 minutes before imaging sessions.

3.2 Results

Rhabdomeric Responses Depend on Adaptation State

Rhabdomeric responses of photoreceptors in the fruit fly can be used to estimate opsin sensitivity, as rhabdomeres are the location where phototransduction takes place after photons are absorbed [113]. To test if *Drosophila* opsin sensitivities shift when adapted to different background conditions, I aimed to perform two-photon calcium imaging to measuring rhabdomeric tuning in both R7 and R8 photoreceptors. In vivo two-photon imaging of genetically targeted GCaMP6f in R7 and R8 photoreceptors allows for straightforward measurement of their axonal outputs in the M6 and M3 layers of the medulla, respectively (Figure 17B). However, I could not visualize rhabdomeres in the eye with my imaging setup and could therefore not directly measure rhabdomeric responses. Instead, I used genetic tools to make indirect measurements of putative rhabdomeric responses (method described in [65]).

I first measured putative rhabdomeric responses in yR7 and yR8 to full-field steps from six LEDs: deep UV, UV, violet, blue, lime, and orange (Figure 17D-E). Flies were either dark-adapted, or adapted to a simulated dawn or morning spectrum at an intensity of 1uE (Figure 17F). The raw putative rhabdomeric responses to LED flashes show clear differences between background conditions, (Figure 18, 20B-20C, black, magenta and orange traces). In yR7, the different background illuminants elicit significantly different degrees

of excitation to dUV, violet, and blue (Figure 18 and Figure 20B). In yR8, the different background illuminants elicit significantly different degrees of excitation to all LEDs. More specifically, in the dark-adapted state, the yR8 rhabdomeric responses is stronger than both light-adapted states across all LED colors except for green, in which the dark- and dawn-adapted responses are not significantly different. This result is easily visualized in the individual flash responses (Figure 18, black traces vs orange and pink traces). Thus, adaptation state affects opsin sensitivities, as demonstrated by the putative rhabdomeric responses in yR7 and yR8.

Differences Due to Adaptation State are Reduced at the Level of Photoreceptor Axons

Next, I measured wild type yR7 and yR8 axonal responses in flies adapted to darkness, the dawn spectrum, or the morning spectrum. Here, the responses to the six LED steps are more similar than at the rhabdomeric level (Figure 19, Figure 20D-E). For yR7, only the green LED elicits a significantly different response across backgrounds, with dawn-adapted flies exhibiting inhibition to green. For yR8, responses in flies adapted to different background spectra are different for three LED colors (UV, violet and blue, Figure 19 and Figure 20E), as opposed to the rhabdomeric responses, which showed variation across all LED steps. Some of the differences at the axonal level could also be accounted

for based on the inability for GCaMP to capture inhibitory signaling under certain conditions. For example, in the dark condition, there is no baseline excitation in photoreceptors, and thus inhibitory mechanisms are nearly impossible to capture as decreases in GCaMP cannot be measured. Thus, it is likely that axonal responses in yR7 and yR8 are even more similar across background conditions than it appears from the GCaMP signal. To answer this directly, future experiments can be done in which mixtures of LEDs are presented while recording from photoreceptors. Thus, the mixtures of excitatory and inhibitory would enable the inhibition to be fully captured.

Figure 18. Putative Rhabdomeric Responses in Three Adaptation States

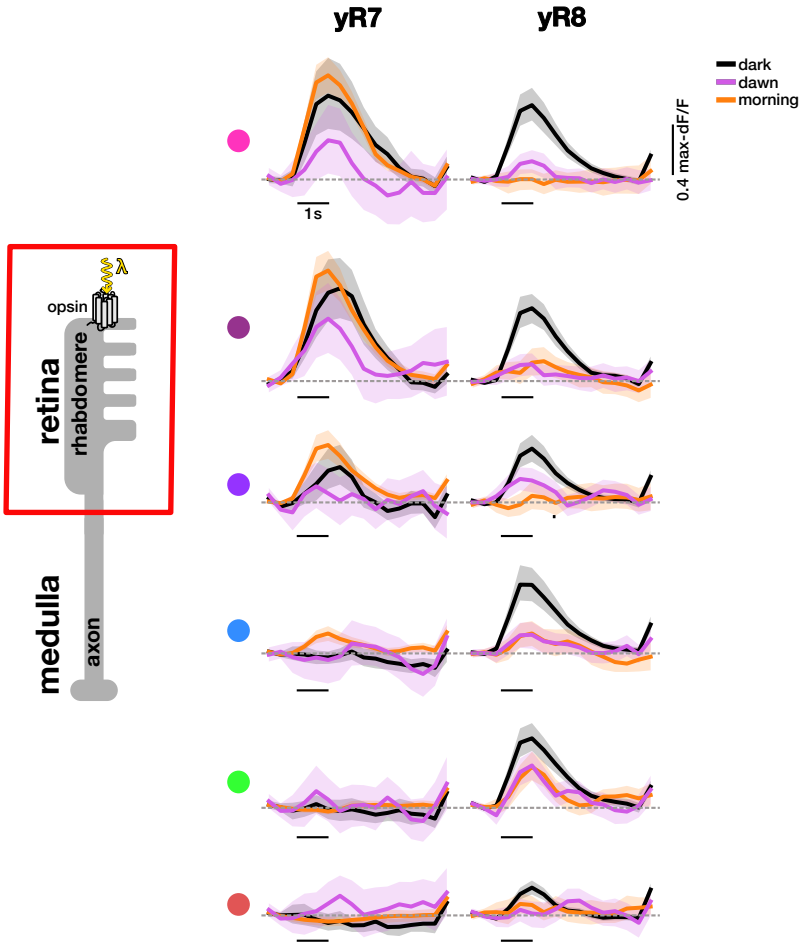

In Drosophila photoreceptors, light (λ) is absorbed in the retina by rhodopsin molecules at the level of the rhabdomeres, where phototransduction takes place. Photoreceptors project their axons to the medulla where synaptic interactions occur. These responses are putative rhabdomeric responses, as indicated by the red box. Here, we see yR7 and yR8 putative responses to full-field flashes of 6 LEDs at an intensity of 0.3 μE. LEDs are identified by the colored circles which correspond to the LEDs in Figure 17D-E. Black, magenta, and orange lines represent the mean photoreceptor response in flies adapted to darkness, a dawn spectrum, and a morning spectrum, respectively. Shaded region represents the 95% confidence interval. Dashed gray lines represent baseline fluorescence. Regions of interest (ROIs) correspond to individual cells, whose responses were averaged equally across flies. For yR7, N = 62 ROIs (5 flies), 137 (7) and 67 (5), respectively. For yR8, N= 174 ROIs (6 flies), 173 (6) and 58 (7), respectively.

Figure 19. Axonal Photoreceptor Responses in Three Adaptation States

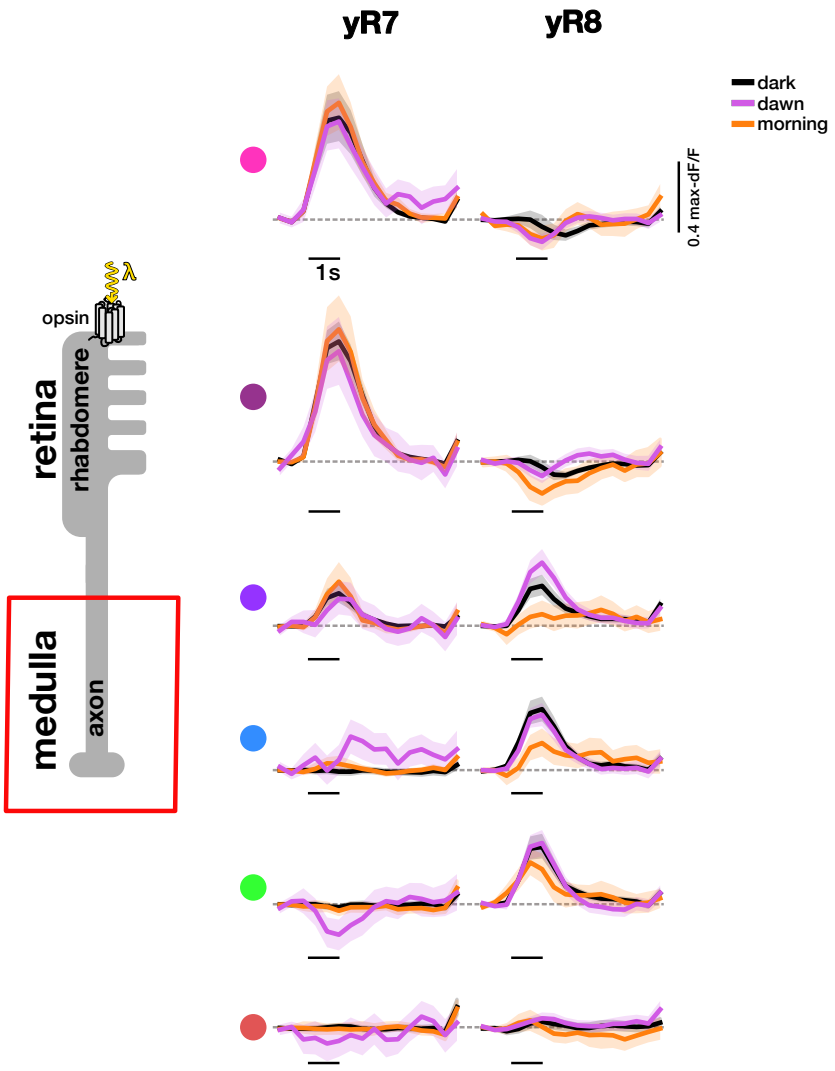

These responses are axonal, as indicated by the red box. Here, we see yR7 and yR8 putative responses to full-field flashes of 6 LEDs at an intensity of 0.3 µE. LEDs are identified by the colored circles which correspond to the LEDs in Figure 17D-E. Black, magenta, and orange lines represent the mean photoreceptor response in flies adapted to darkness, a dawn spectrum, and a morning spectrum, respectively. Shaded region represents the 95% confidence interval. Dashed gray lines represent baseline fluorescence. Regions of interest (ROIs) correspond to individual cells, whose responses were averaged equally across flies. For yR7, N = 184 ROIs (5 flies), 222 (5) and 89 (4), respectively. For yR8, N= 471 (9), 176 (5), and 104 (4), respectively.

Figure 20. Photoreceptor Responses Vary Across Adaptation States

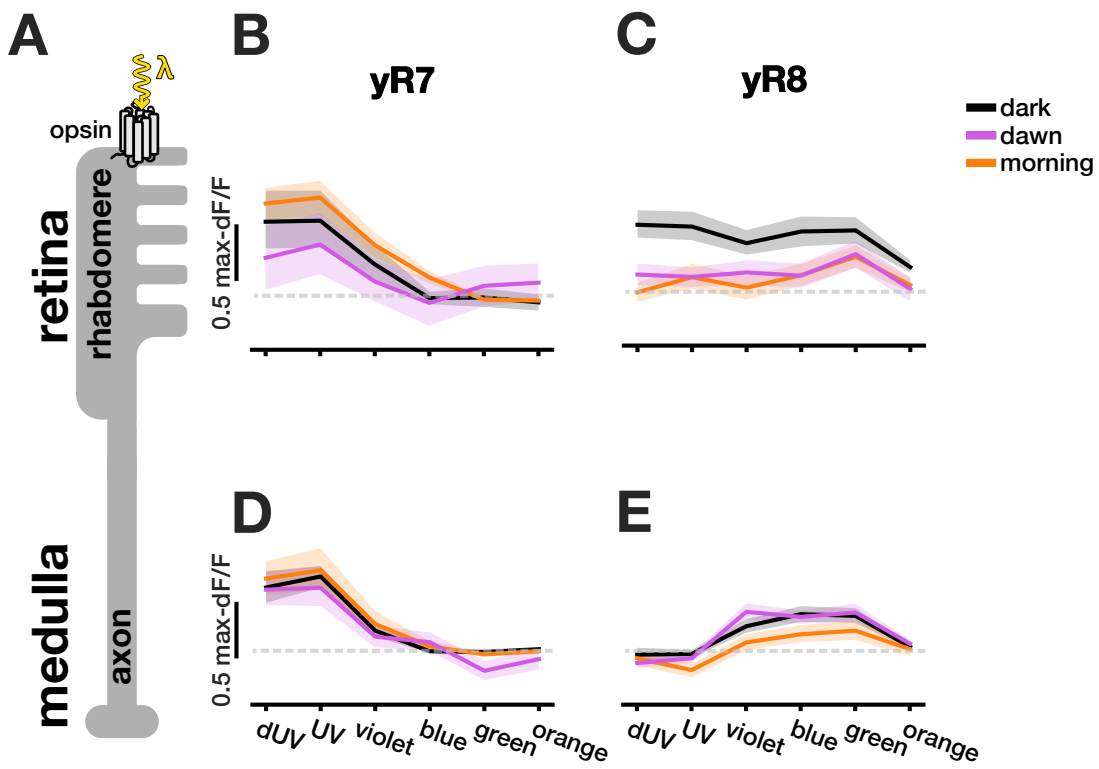

(A) In Drosophila photoreceptors, light (λ) is absorbed in the retina by rhodopsin molecules at the level of the rhabdomeres, where phototransduction takes place. Photoreceptors project their axons to the medulla where synaptic interactions occur. (B–C) Plots show amplitudes drawn from measured max-normalized responses of yR7 and yR8 axons to 0.3 µE flashes from six LEDs. Black, magenta, and orange lines represent the mean photoreceptor response in flies adapted to darkness, a dawn spectrum, and a morning spectrum, respectively. Shaded region represents the 95% confidence interval. Dashed gray lines represent baseline fluorescence. For yR7, N = 62 ROIs (5 flies), 137 (7) and 67 (5), respectively. For yR8, N= 174 ROIs (6 flies), 173 (6) and 58 (7), respectively. (D–E) Amplitudes drawn from measured max-normalized responses of yR7 and yR8 axons to 0.3 µE flashes from six LEDs. Constructed using the amplitudes of measured responses of R7 and R8 axons in wild-type flies. For yR7, N = 184 ROIs (5 flies), 222 (5) and 89 (4), respectively. For yR8, N= 471 (9), 176 (5), and 104 (4), respectively.

3.3 Discussion

Here, I show that yR7 and yR8 putative rhabdomeric and axonal responses vary based on background adaptation state. However, responses to single LED flashes vary more at the rhabdomeric level than the axonal level. This suggests that shifts in opsin sensitivities due to background illuminants are partially rectified at the axonal level in photoreceptors, most likely through circuit interactions. To determine if this is the case, future work is necessary to extrapolate sensitivity curves from flash responses. This would provide putative opsin sensitivity curves and axonal tuning curves to more closely examine the effect of adaptation state on chromatic encoding at various levels of color circuitry.

Differences in *Drosophila* opsin sensitivities based on adaptation to various background illuminants could have multiple implications. On one hand, these differences could be maintained in downstream cells, and ultimately affect perception- similar to the purkinje shift in mammals, where peak sensitivity to light shifts to shorter wavelengths under dark-adapted conditions [114]. Alternatively, downstream neurons could account for opsin sensitivity shifts through circuit mechanisms to normalize perception across background conditions, which is already partially achieved by the rhabdomeric to axonal signal transformation. To determine if the fruit fly visual system is utilizing one

or both of these strategies, spectral tuning of downstream neurons must be measured in flies adapted to multiple spectral compositions.

3.4 Methods

For details on the experimental model, two-photon calcium imaging, visual stimulation, and statistical analysis, see ***Chapter 2.3.***

Chapter 4: Future Directions

4.1 Introduction

Over the years, my exploration into color vision circuitry in flies lead me to investigate avenues in which I never gleaned enough data to draw solid, detailed conclusions. However, I believe it is important to include these data for the interest of those in the field. Below, you will find both preliminary data along with discussion of concepts of color vision in *Drosophila*, which will hopefully provide a basis for follow-up studies in the future.

4.2 Chromatic Circuits in the Optic Lobe

As previously described, spectral opponency at the level of photoreceptor axons is achieved through direct axo-axonal synapses, and by lateral interactions mediated the medulla neuron Dm9. Until recently, Dm9 was the only postsynaptic partner of R7 and R8 to be functionally characterized. However, new studies show that Dm8, a direct postsynaptic partner of R7, demonstrates spatio-chromatic opponent properties [115, 116]. Moreover, these studies show that the outer photoreceptors R1-6 also shape the response properties of Dm8. Thus, at this early processing stage, spatial, spectral, and luminance information are already converging to give rise to complex processing strategies in the fruit fly. What are the next steps in unraveling these chromatic circuits in the optic lobe?

Looking at photoreceptor signaling properties themselves, it is still unclear if they exhibit center-surround properties as predicted our circuit model (See Chapter 2). In Figure 16, I showed results from presentation of patterned stimuli which suggest surround opponency in yR8. However, further experiments are necessary to characterize these receptive field properties. Not only are the spatial properties of pR8 and R7 receptive fields unknown, general spatio-chromatic properties of R7s and R8s remain unexplored. To get at the interaction between spectral and spatial information at the level of the photoreceptors, it would be informative to measure single photoreceptor

responses to both colored spots that stimulate the center, and colored annuli that stimulate the surround. Moreover, these experiments can be completed in different regimens of light to probe for possible intensity-dependent differences in receptive field size, a well characterized property observed in the vertebrate retina.

Looking deeper into the optic lobe, there are numerous cell types likely be involved in color processing based on their anatomical connectivity. Many interesting questions particular remains, such as: how early does hue selectivity and/or intensity invariance arise in the brain of the fruit fly? To determine this, a survey of chromatic properties of many medulla and lobula neurons must be completed.

4.3 Higher Order Color Processing in *Drosophila*

Investigating the Potential for Color Constancy in Flies

It has been shown in a variety of species that the gain of narrow-band photoreceptors depends on the spectral composition of both the local and surrounding stimulus [117]. This processing property is thought to be what enables the color constancy phenomenon to exist, in which organisms have the ability to perceive the color of objects as having the same appearance regardless of the global illuminant wavelength. This phenomenon is clearly a

compensation made by the brain, as local illuminants drastically change the perception of color. One mechanism to explain this gain-dependency is spatially and spectrally broad feedback onto photoreceptors. This feedback is likely mediated by horizontal cells [118, 119]. For example, in an environment with a red global illuminant, blue-sensitive photoreceptors would not be activated, but the negative feedback signal from horizontal cells would increase their gain. Conversely, red-sensitive photoreceptors would be directly stimulated by the illuminant, which would decrease their gain. These changes together would serve to compensate for the global red light by strengthening the blue signal and weakening the red signal, and thus color constancy would be maintained.

While color constancy is commonly thought of as requiring a complex neural system, it has actually been shown that the honeybees and bumblebees can maintain color constancy despite large spectral changes in the illuminant [120, 121]. While color constancy has not been explored in *Drosophila*, my recent discovery of Dm9-mediated indirect spatial opponency in R7 and R8 led me to hypothesize that global illuminance affects the gain of photoreceptors through this feedback mechanism. To test this, I measured calcium responses in pR7 to increasing intensity UV flashes in flies adapted to different background conditions. Constructing curves from response amplitudes in each condition would allow me to determine if there were changes in gain based on global illumination. To enable proper measurements of response amplitude, it is

important to establish an accurate baseline across spectrally varying illuminant conditions. In all experiments, I first adapted flies to a "white background," or a mixture of UV (340nm), blue (465 nm) and green (565 nm) LED presentations which summed to 0.5 nW/mm2. This ensured that all photoreceptors were activated at a base level before the start of the stimulus. As different background illuminants can depress R7 activation, this baseline excitation was necessary to fully capture this depression via calcium imaging. In addition, I layered full-field UV, blue, or green on top of the white background at varying intensities (see Figure 21 for details). I presented 0.5 second full-field flashes of UV at 20 nW/mm^2, which is the preferred activating stimulus for pR7. I did this for each background condition, and then built curves for each condition based on the UV step intensity. Comparing the slope of these curves revealed changes in gain when additional colors were present in the background illuminant, as compared to the white background. More specifically, the presence of UV in the global illuminant increased baseline excitation and thus reduced the amplitude of pR7 responses to UV. Furthermore, the presence of UV reduced the slope of the corresponding curves, indicating a decrease in gain. Conversely, the presence of blue and green in the global illuminant decreased pR7 baseline excitation while still allowing for large amplitude responses, which resulted in steeper slopes in the corresponding curves. As isolated photoreceptors cannot reduce their own baseline excitation in responses to added luminance, this indicates that circuit

mechanisms are enabling these gain changes. Moreover, as I have previously shown that any effects of green light on pR7 are mediated through Dm9, the gain change in pR7 with a green global illuminant further supports the hypothesis that lateral circuit interactions underlie possible color constancy in the fruit fly. Altogether, these data indicated that the gain R7s and R8s in *Drosophila* are affected by the spectral composition of the global illuminant, and that this system is likely poised to confer the functionality necessary for color constancy.

One caveat to consider, however, is that one can only truly probe for color constancy mechanisms by contrasting both local and global illuminants. While my experiments showed a change in gain, they did not get to the heart of the test for color constancy. Due to experimental limitations, the UV steps presented to test R7 responsivity in various background conditions was also full-field. In an ideal scenario, the UV flash would have only activated responses in a single ommatidium- which I could image under various full-field background conditions. Thus, future experiments using a custom UV/G/B projector would provide even stronger evidence that color constancy is possible for the fruit fly, and is likely made possible by Dm9-mediated spatial opponency in R7s and R8s.

Figure 21. Spectral Composition of Global Illumination Affects Photoreceptor Gain

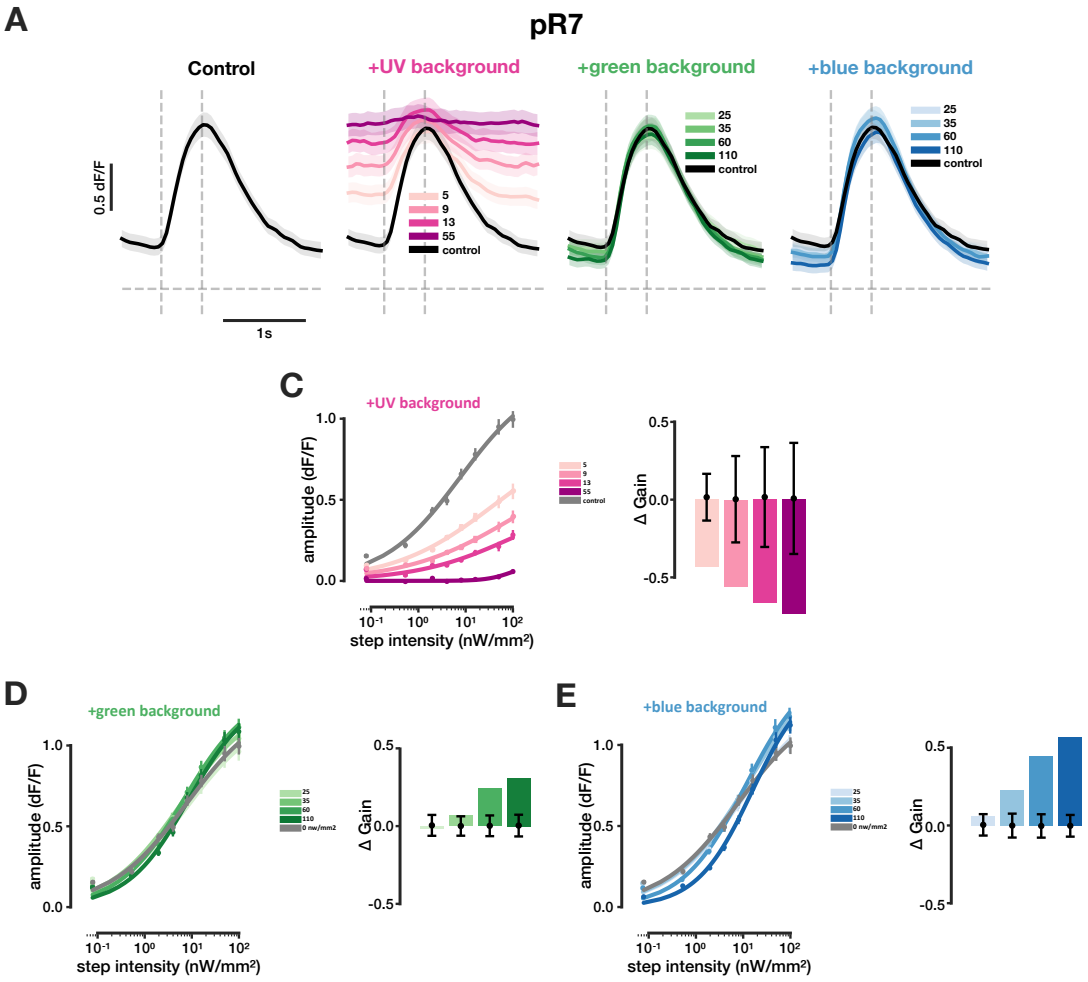

(A) Average GCaMP6f responses of pR7 in wild-type flies to 0.5s UV flashes when adapted to three different background spectra at multiple intensities. Flies were adapted to a "white" background, or an equivalent intensity of the UV, blue and green LEDs summing to 0.5 nW/mm^2, and one additional background component of either UV, blue, or green. Vertical dashed gray lines represent onset and offset of light presentation. Horizontal dashed gray line represents baseline. (B) Amplitude of pR7 responses at increasing step intensities, when flies are adapted to simply the white background (grey) or the white background with additional UV background illumination at four intensities (5, 9, 13, and 55 nW/mm^2, magenta traces). Gain is represented as the difference between slopes in the background amplitude curve and the curves constructed at each UV background condition. (C-D) Same as (B), but with green and blue background illumination, respectively. Background intensities included 25, 35, 60, and 100 nW/mm^2

Exploring the Role of Spectral Information in Navigation

After exploring mechanisms of spatial and chromatic opponency at the level of the photoreceptors, I wanted to determine how these signals were transformed one synapse downstream. While local medulla cells downstream of R7 had already been identified by electron microscopy [58, 122], projection neurons that terminate in higher order neuropils have not been included in these studies.

To isolate undescribed post-synaptic partners of R7, I used an anterograde, proximity-based tracing technique called trans-Tango[123]. This technique works by global expression of a synthetic signaling pathway in all neurons, combined with cell-type specific expression of the tethered ligand that activates this pathway. By expressing the ligand in R7 photoreceptors, I was able to initiate the signaling pathway in its putative downstream partners. I identified multiple pathways with dendrites in close proximity to R7 and projections terminating in various higher order neuropils (Figure 22A).

Interestingly, I identified a pathway with dense projections to the Anterior Optic Tubercle (AOTu), a region known to be crucial for navigation in insects. This pathway seemed to be specific to R7 photoreceptors, as I did not identify it in R8 trans-Tango experiments (data not shown). Based on anatomical studies, I identified this pathway as consisting of MeTu neurons: a class of cell types with various projection patterns from layer 6 of the medulla neuropil to the small unit

of the AOTu (Figure 22B) [124]. This was confirmed by the same R7 trans-Tango experiments performed by Timaeus et. al [125]. MeTu cells have been shown to carry polarization information from the medulla to the AOTu [126]. Across other insect species, the AOTu is known combine this e-vector information with other celestial cues, such as the balance of UV and green light, to effectively serve as a sky compass [127]. Moreover, color opponency has been observed in the AOTu of bumblebees [128], and also in cells projecting to AOTu in locusts [129, 130]. Thus, as MeTu cells are the likely candidates to transmit chromatic information to the AOTu, I wanted to test if these cells simply relayed opponent information, or if a signal transformation immediately took place at the level of the medulla.

To test this, I performed two-photon calcium imaging on MeTu dendrites in the medulla while presenting stimuli that allowed me to measure the spectral tuning of these neurons across the wavelength spectrum (see Methods and Chapter 1). By clustering the responses using k-means clustering, I found a variety of responses already present at the medulla level (Figure 22C, pink, blue and green traces). More specifically, I observed broadband responses (green trace), narrow band responses (pink trace), and opponent responses (blue trace). Thus, the opponent signal from R7 photoreceptors is already transformed at the level of the medulla. Future experiments will be crucial to ascertain if and how

this chromatic information is integrated with polarization information in the AOTu of *Drosophila* to form an effective sky compass.

Figure 22. Cell Types Downstream of R7 Exhibit Spectrally Complex Responses

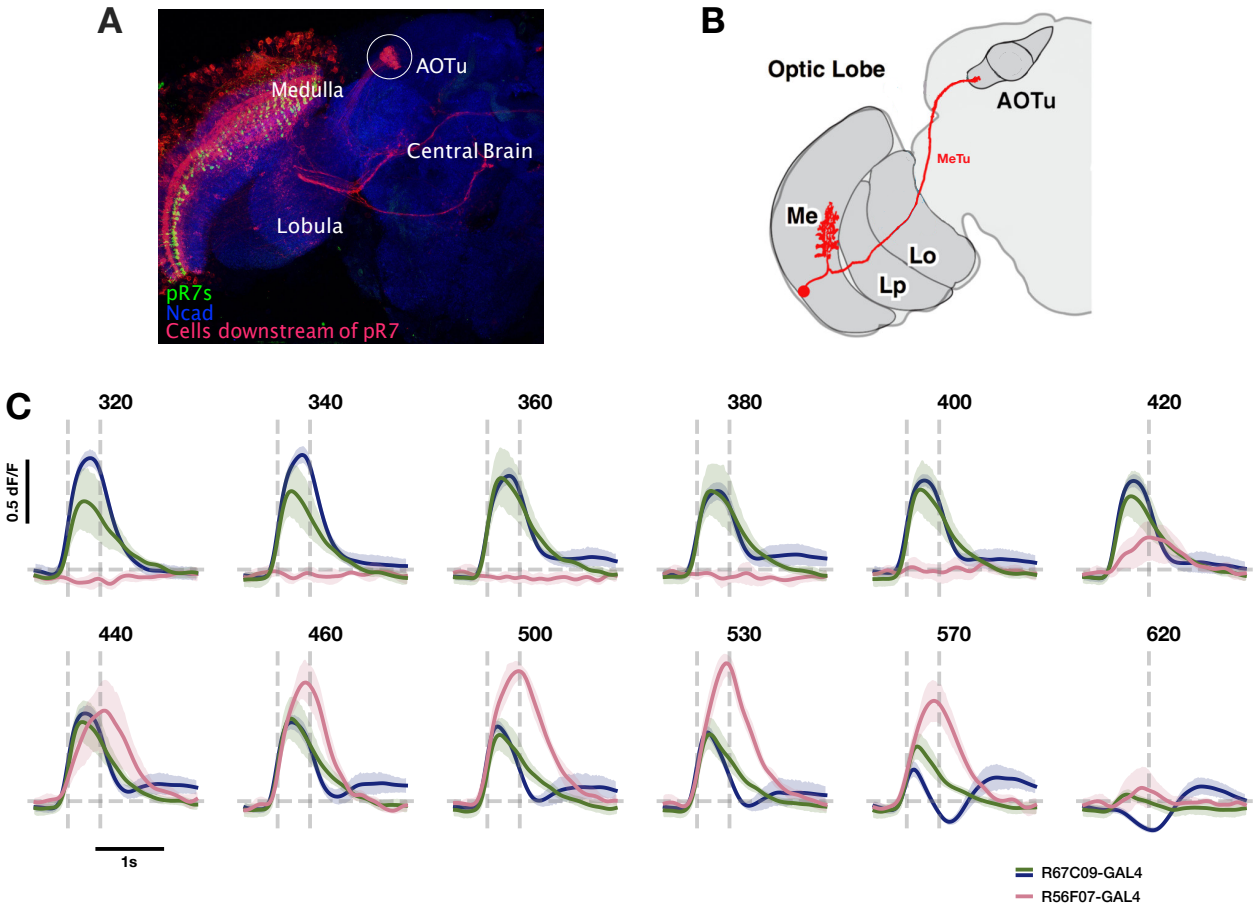

(A) Trans-tango tracing of postsynaptic partners to pR7s. Notably, I identified a pathway downstream of R7s with dense projections directly to the AOTu, which I presume to be MeTu subtypes. (B) MeTu cells project directly from the photoreceptor level in the medulla to the lateral AOTu. (Modified from [131]) (C) Max-normalized, clustered calcium responses of MeTu dendrites measured to 1s simulated wavelengths presentations (R56F07-GAL4 and R67C09-GAL4 driving GCaMP6f, N= 2 and 3 flies, respectively).

Representation of Color in the Mushroom Body

Understanding basic opponent mechanisms in the optic lobe of the fruit fly is merely one building block in explaining color processing as a whole. A fascinating question in the field is how chromatic information is used by *Drosophila* to guide behavioral output. An understanding of how spectral information is assigned valence and associated with other sensory information is crucial to start to answer this question. The mushroom body has been shown to be the main locus of learning and memory in *Drosophila,* and has been extensively studied in the context of olfactory learning [132]. However, it is unknown how chromatic information is represented in the mushroom body, even though it has been shown that fruit flies require the mushroom body to complete color learning tasks successfully [133, 134]. Moreover, the mechanisms of sensory integration in the mushroom body remain largely unexplored. Future experiments, both functional and behavioral, can elucidate the extent of multi-sensory memory in the fruit fly, and shed light on how chromatic information is encoded in the mushroom body.

4.3. Discussion

As mentioned in this chapter, chromatic information is likely used by the *Drosophila* for purposes such as navigation and color constancy. However, there are numerous other hypotheses regarding the ecological relevance of color for the fruit fly. For example, it has been proposed that a comparison between UV and visible wavelengths enables identification of ripe fruit[135] and horizon stabilization during flight [136]. It has also been shown that daytime color preference in Drosophila depends on the circadian clock [137], and moreover, that R8 photoreceptors have been shown to play a role in circadian entrainment [87].

As compared to other insects such as the butterfly and the honey bee, relatively little is known about the behavioral relevance of color to fruit fly. However, the recent interest in *Drosophila* as a tractable model for color vision will likely propel our understanding in this realm forward. Moreover, studies in the relatively simple brain of the fruit fly will allow us to identify convergent solutions to the complex problem of encoding the rich chromatic information which exists in the world around us.

4.4 Methods

Trans-tango experiments were performed using flies gifted by Gilead Barnea. In these flies, which the trans-Tango construct containing ligand, synthetic receptor and hArr::TEV genes was incorporated at the attP40 site. The construct containing the reporter genes, UAS-myrGFP and QUAS-mtdTomato(3xHA), was incorporated at the su(Hw)attP8 site. The conditional suppressor construct, tubP-FRT-QS-FRT, was incorporated at the VK00018 site[123]. The UAS constructs were driven by a panR7-GAL4 construct (gifted by Claude Desplan).

For further details on the experimental model, two-photon calcium imaging, visual stimulation, immunohistochemistry, and statistical analysis, see ***Chapter 2.3.***

References

1. Osorio, D. and M. Vorobyev, *A review of the evolution of animal colour vision and visual communication signals.* Vision Res, 2008. **48**(20): p. 2042-51.

2. Conway, B.R., et al., *Advances in color science: from retina to behavior.* J Neurosci, 2010. **30**(45): p. 14955-63.

3. Rushton, W., *Pigments and signals in colour vision.* The Journal of physiology, 1972. **220**(3): p. 1P.

4. Hardie, R.C. and P. Raghu, *Visual transduction in Drosophila.* Nature, 2001. **413**(6852): p. 186-193.

5. Kelber, A. and G.H. Jacobs, *Evolution of Color Vision*, in *Human Color Vision*, J. Kremers, R.C. Baraas, and N.J. Marshall, Editors. 2016, Springer International Publishing: Cham. p. 317-354.

6. Solomon, S.G. and P. Lennie, *The machinery of colour vision.* Nat Rev Neurosci, 2007. **8**(4): p. 276-86.

7. Barlow, H.B., *What causes trichromacy? A theoretical analysis using comb-filtered spectra.* Vision Research, 1982. **22**(6): p. 635-643.

8. Collin, S.P., et al., *The evolution of early vertebrate photoreceptors.* Philosophical Transactions of the Royal Society B: Biological Sciences, 2009. **364**(1531): p. 2925-2940.

9. Thoen, H.H., et al., *A Different Form of Color Vision in Mantis Shrimp.* Science, 2014. **343**(6169): p. 411.

10. Zaidi, Q., et al., *Evolution of neural computations: Mantis shrimp and human color decoding.* Iperception, 2014. **5**(6): p. 492-6.

11. Hurvich, L.M. and D. Jameson, *An opponent-process theory of color vision.* Psychological review, 1957. **64**(6p1): p. 384.

12. Jacobs, G.H., *The discovery of spectral opponency in visual systems and its impact on understanding the neurobiology of color vision.* Journal of the History of the Neurosciences, 2014. **23**(3): p. 287-314.

13. Tuten, W.S., et al., *Spatiochromatic Interactions between Individual Cone Photoreceptors in the Human Retina.* The Journal of Neuroscience, 2017. **37**(39): p. 9498.

14. Thoreson, W.B. and S.C. Mangel, *Lateral interactions in the outer retina.* Progress in retinal and eye research, 2012. **31**(5): p. 407-441.

15. Twig, G., H. Levy, and I. Perlman, *Color opponency in horizontal cells of the vertebrate retina.* Progress in retinal and eye research, 2003. **22**(1): p. 31-68.

16. Dacey, D.M. and O.S. Packer, *Colour coding in the primate retina: diverse cell types and cone-specific circuitry.* Current opinion in neurobiology, 2003. **13**(4): p. 421-427.

17. Crook, J.D., et al., *Horizontal Cell Feedback without Cone Type-Selective Inhibition Mediates "Red-Green" Color Opponency in Midget Ganglion Cells of the Primate Retina.* The Journal of Neuroscience, 2011. **31**(5): p. 1762.

18. McMahon, M.J., O. Packer, and D.M. Dacey, *Circuitry of the Parasol Ganglion Cell Receptive Field Surround.* Investigative Ophthalmology & Visual Science, 2003. **44**(13): p. 3236-3236.

19. Packer, O.S., et al., *Blue-yellow opponency in primate S cone photoreceptors.* The Journal of neuroscience : the official journal of the Society for Neuroscience, 2010. **30**(2): p. 568-572.

20. Joesch, M. and M. Meister, *A neuronal circuit for colour vision based on rod-cone opponency.* Nature, 2016. **532**(7598): p. 236-9.

21. Derrington, A.M., J. Krauskopf, and P. Lennie, *Chromatic mechanisms in lateral geniculate nucleus of macaque.* The Journal of Physiology, 1984. **357**(1): p. 241-265.

22. Valberg, A., *Unique hues: an old problem for a new generation.* Vision Res, 2001. **41**(13): p. 1645-57.

23. Webster, M.A., et al., *Variations in normal color vision. II. Unique hues.* Journal of the Optical Society of America A, 2000. **17**(9): p. 1545-1555.

24. Buchsbaum, G., A. Gottschalk, and H.B. Barlow, *Trichromacy, opponent colours coding and optimum colour information transmission in the retina.* Proceedings of the Royal Society of London. Series B. Biological Sciences, 1983. **220**(1218): p. 89-113.

25. Solomon, S.G., *Chapter 3 - Retinal ganglion cells and the magnocellular, parvocellular, and koniocellular subcortical visual pathways from the eye to the brain*, in *Handbook of Clinical Neurology*, J.J.S. Barton and A. Leff, Editors. 2021, Elsevier. p. 31-50.

26. Gegenfurtner, K.R. and D.C. Kiper, *Color vision.* Neuroscience, 2003. **26**(1): p. 181.

27. Hubel, D.H. and T.N. Wiesel, *Receptive fields and functional architecture of monkey striate cortex.* J Physiol, 1968. **195**(1): p. 215-43.

28. Desimone, R., et al., *Contour, color and shape analysis beyond the striate cortex.* Vision Res, 1985. **25**(3): p. 441-52.

29. Komatsu, H., *Mechanisms of central color vision.* Current Opinion in Neurobiology, 1998. **8**(4): p. 503-508.

30. Zeki, S. and L. Marini, *Three cortical stages of colour processing in the human brain.* Brain: A Journal of Neurology, 1998. **121**(9): p. 1669-1685.

31. Conway, B.R., S. Moeller, and D.Y. Tsao, *Specialized color modules in macaque extrastriate cortex.* Neuron, 2007. **56**(3): p. 560-73.

32. Matsumora, T., K. Koida, and H. Komatsu, *Relationship between color discrimination and neural responses in the inferior temporal cortex of the monkey.* J Neurophysiol, 2008. **100**(6): p. 3361-74.

33. Harada, T., et al., *Distribution of colour-selective activity in the monkey inferior temporal cortex revealed by functional magnetic resonance imaging.* Eur J Neurosci, 2009. **30**(10): p. 1960-70.

34. Yasuda, M., T. Banno, and H. Komatsu, *Color selectivity of neurons in the posterior inferior temporal cortex of the macaque monkey.* Cereb Cortex, 2010. **20**(7): p. 1630-46.

35. Conway, B.R. and D.Y. Tsao, *Color-tuned neurons are spatially clustered according to color preference within alert macaque posterior inferior temporal cortex.* Proc Natl Acad Sci U S A, 2009. **106**(42): p. 18034-9.

36. Von Frisch, K., *Der farbensinn und formensinn der biene*. 1914: Рипол Классик.

37. Song, B.-M. and C.-H. Lee, *Toward a Mechanistic Understanding of Color Vision in Insects.* Frontiers in Neural Circuits, 2018. **12**(16).

38. Schnaitmann, C., et al., *Color Processing in the Early Visual System of Drosophila.* Cell, 2018. **172**(1-2): p. 318-330.e18.

39. Schnaitmann, C., et al., *Color Discrimination with Broadband Photoreceptors.* Current Biology, 2013. **23**(23): p. 2375-2382.

40. Gao, S., et al., *The neural substrate of spectral preference in Drosophila.* Neuron, 2008. **60**(2): p. 328-42.

41. Melnattur, K.V., et al., *Multiple Redundant Medulla Projection Neurons Mediate Color Vision in Drosophila.* Journal of neurogenetics, 2014(0): p. 1-15.

42. Karuppudurai, T., et al., *A Hard-Wired Glutamatergic Circuit Pools and Relays UV Signals to Mediate Spectral Preference in Drosophila.* Neuron, 2014. **81**(3): p. 603-615.

43. Yamaguchi, S., C. Desplan, and M. Heisenberg, *Contribution of photoreceptor subtypes to spectral wavelength preference in Drosophila.* Proceedings of the National Academy of Sciences, 2010. **107**(12): p. 5634-5639.

44. Fischbach, K.F., *Simultaneous and successive colour contrast expressed in "slow" phototactic behaviour of walkingDrosophila melanogaster.* Journal of comparative physiology, 1979. **130**(2): p. 161-171.

45. Heisenberg, M. and E. Buchner, *The role of retinula cell types in visual behavior of Drosophila melanogaster.* Journal of comparative physiology, 1977. **117**(2): p. 127-162.

46. Hardie, R.C., *Functional Organization of the Fly Retina*, in *Progress in Sensory Physiology*, H. Autrum, et al., Editors. 1985, Springer Berlin Heidelberg: Berlin, Heidelberg. p. 1-79.

47. Behnia, R. and C. Desplan, *Visual circuits in flies: beginning to see the whole picture.* Current opinion in neurobiology, 2015. **34**: p. 125-132.

48. Clandinin, T.R. and S.L. Zipursky, *Afferent Growth Cone Interactions Control Synaptic Specificity in the Drosophila Visual System.* Neuron, 2000. **28**(2): p. 427-436.

49. Salcedo, E., et al., *Blue-and green-absorbing visual pigments of Drosophila: Ectopic expression and physiological characterization of the R8 photoreceptor cell-specific Rh5 and Rh6 rhodopsins.* The Journal of Neuroscience, 1999. **19**(24): p. 10716-10726.

50. Govardovskii, V.I., et al., *In search of the visual pigment template.* Vis Neurosci, 2000. **17**(4): p. 509-28.

51. Shevell, S.K. and P.R. Martin, *Color opponency: tutorial.* Journal of the Optical Society of America. A, Optics, image science, and vision, 2017. **34**(7): p. 1099-1108.

52. Su, C.-Y., et al., *Non-synaptic inhibition between grouped neurons in an olfactory circuit.* Nature, 2012. **492**(7427): p. 66-71.

53. Wernet, M.F., et al., *Genetic Dissection Reveals Two Separate Retinal Substrates for Polarization Vision in Drosophila.* Current Biology, 2012. **22**(1): p. 12-20.

54. Kelber, A., M. Vorobyev, and D. Osorio, *Animal colour vision — behavioural tests and physiological concepts.* Biological Reviews, 2003. **78**(1): p. 81-118.

55. Renoult, J.P., A. Kelber, and H.M. Schaefer, *Colour spaces in ecology and evolutionary biology.* Biological Reviews, 2017. **92**(1): p. 292-315.

56. Henderson, S.R., H. Reuss, and R.C. Hardie, *Single photon responses in Drosophila photoreceptors and their regulation by Ca2+.* The Journal of Physiology, 2000. **524**(1): p. 179-194.

57. Juusola, M. and R.C. Hardie, *Light adaptation in Drosophila photoreceptors: I. Response dynamics and signaling efficiency at 25 degrees C.* J Gen Physiol, 2001. **117**(1): p. 3-25.

58. Takemura, S.-y., et al., *A visual motion detection circuit suggested by Drosophila connectomics.* Nature, 2013. **500**(7461): p. 175-181.

59. Davis, F.P., et al., *A genetic, genomic, and computational resource for exploring neural circuit function.* eLife, 2020. **9**: p. e50901.

60. Reiser, M., *colorVision2.pdf.* Janelia Research Campus. Poster, 2019.

61. Ukani, N.H., et al., *NeuroNLP: a natural language portal for aggregated fruit fly brain data.* bioRxiv, 2016: p. 092429.

62. Nern, A., B.D. Pfeiffer, and G.M. Rubin, *Optimized tools for multicolor stochastic labeling reveal diverse stereotyped cell arrangements in the fly visual system.* Proceedings of the National Academy of Sciences, 2015. **112**(22): p. E2967-E2976.

63. Klapoetke, N.C., et al., *Independent optical excitation of distinct neural populations.* Nat Methods, 2014. **11**(3): p. 338-46.

64. Fisher, Y.E., et al., *A Class of Visual Neurons with Wide-Field Properties Is Required for Local Motion Detection.* Curr Biol, 2015. **25**(24): p. 3178-89.

65. Heath, S.L., et al., *Circuit Mechanisms Underlying Chromatic Encoding in Drosophila Photoreceptors.* Current Biology, 2020. **30**(2): p. 264-275.e8.

66. Takemura, S.-y., et al., *Synaptic circuits and their variations within different columns in the visual system of Drosophila.* Proceedings of the National Academy of Sciences, 2015. **112**(44): p. 13711-13716.

67. Cooper, B., B.B. Lee, and D. Cao, *Macaque retinal ganglion cell responses to visual patterns: harmonic composition, noise, and psychophysical detectability.* Journal of Neurophysiology, 2016. **115**(6): p. 2976-2988.

68. Dacey, D., et al., *Center surround receptive field structure of cone bipolar cells in primate retina.* Vision Research, 2000. **40**(14): p. 1801-1811.

69. Fisher, T.G., H.J. Alitto, and W.M. Usrey, *Retinal and Non-Retinal Contributions to Extraclassical Surround Suppression in the Lateral Geniculate Nucleus.* The Journal of Neuroscience, 2016.

70. Barlow, H.B., *Possible principles underlying the transformations of sensory messages.* Possible Principles Underlying the Transformation of Sensory Messages, 1961: p. 217-234.

71. Atick, J.J. and A.N. Redlich, *What does the retina know about natural scenes?* Neural Computation, 1992. **4**(2): p. 196-210.

72. Vorobyev, M., et al., *Colour thresholds and receptor noise: behaviour and physiology compared.* Vision Res, 2001. **41**(5): p. 639-53.

73. Scheffer, L.K. and I.A. Meinertzhagen, *The Fly Brain Atlas.* Annual Review of Cell and Developmental Biology, 2019. **35**(1): p. 637-653.

74. Stavenga, D., *Angular and spectral sensitivity of fly photoreceptors. II. Dependence on facet lens F-number and rhabdomere type in Drosophila.* Journal of Comparative Physiology A, 2003. **189**(3): p. 189-202.

75. Hardie, R.C., N. Franceschini, and P.D. McIntyre, *Electrophysiological analysis of fly retina.* Journal of comparative physiology, 1979. **133**(1): p. 23-39.

76. Lennie, P., P.W. Haake, and D.R. Williams, *The design of chromatically opponent receptive fields*, in *Computational models of visual processing.* 1991, The MIT Press: Cambridge, MA, US. p. 71-82.

77. Lee, B.B., et al., *Spatial distributions of cone inputs to cells of the parvocellular pathway investigated with cone-isolating gratings.* Journal of the Optical Society of America. A, Optics, image science, and vision, 2012. **29**(2): p. A223-A232.

78. Derrico, J.B. and G. Buchsbaum, *A computational model of spatiochromatic image coding in early vision.* Journal of Visual Communication and Image Representation, 1991. **2**(1): p. 31-38.

79. Atick, J.J., Z. Li, and A.N. Redlich, *Understanding retinal color coding from first principles.* Neural Computation, 1992. **4**(4): p. 559-572.

80. Livingstone, M.S. and D.H. Hubel, *Anatomy and physiology of a color system in the primate visual cortex.* J Neurosci, 1984. **4**(1): p. 309-356.

81. Takeuchi, Y., K. Arikawa, and M. Kinoshita, *Color discrimination at the spatial resolution limit in a swallowtail butterfly, Papilio xuthus.* Journal of Experimental Biology, 2006. **209**(15): p. 2873-2879.

82. Giurfa, M., et al., *Detection of coloured stimuli by honeybees: minimum visual angles and receptor specific contrasts.* Journal of Comparative Physiology A, 1996. **178**(5): p. 699-709.

83. Giurfa, M. and M. Vorobyev, *The angular range of achromatic target detection by honey bees.* Journal of Comparative Physiology A, 1998. **183**(1): p. 101-110.

84. Cook, T., et al., *Distinction between color photoreceptor cell fates is controlled by Prospero in Drosophila.* Dev Cell, 2003. **4**(6): p. 853-64.

85. Saint-Charles, A., et al., *Four of the six Drosophila rhodopsin-expressing photoreceptors can mediate circadian entrainment in low light.* Journal of Comparative Neurology, 2016. **524**(14): p. 2828-2844.

86. Vasiliauskas, D., et al., *Feedback from rhodopsin controls rhodopsin exclusion in Drosophila photoreceptors.* Nature, 2011. **479**(7371): p. 108-112.

87. Alejevski, F., et al., *The HisCl1 histamine receptor acts in photoreceptors to synchronize Drosophila behavioral rhythms with light-dark cycles.* Nature Communications, 2019. **10**(1): p. 252.

88. Tahayato, A., et al., *Otd/Crx, a Dual Regulator for the Specification of Ommatidia Subtypes in the Drosophila Retina.* Developmental Cell, 2003. **5**(3): p. 391-402.

89. Behnia, R., et al., *Processing properties of ON and OFF pathways for Drosophila motion detection.* Nature, 2014. **512**(7515): p. 427-430.

90. Mazzoni, E.O., et al., *Iroquois complex genes induce co-expression of rhodopsins in Drosophila.* PLoS biology, 2008. **6**(4): p. e97.

91. Morante, J. and C. Desplan, *Dissection and staining of Drosophila optic lobes at different stages of development.* Cold Spring Harbor Protocols, 2011. **2011**(6): p. pdb. prot5629.

92. Kries, J.V., *Die Gesichtsempfindungen.* Nagel's Handbuch der Physiologie des Menschen, 1905. **3**: p. 109.

93. Kelber, A. and D. Osorio, *From spectral information to animal colour vision: experiments and concepts.* Proceedings of the Royal Society B: Biological Sciences, 2010. **277**(1688): p. 1617-1625.

94. Giovannucci, A., et al., *CaImAn an open source tool for scalable calcium imaging data analysis.* eLife, 2019. **8**: p. e38173.

95. Chittka, L., et al., *Ultraviolet as a component of flower reflections, and the colour perception of Hymenoptera.* Vision Res, 1994. **34**(11): p. 1489-508.

96. Chittka, L., *Optimal Sets of Color Receptors and Color Opponent Systems for Coding of Natural Objects in Insect Vision.* Journal of Theoretical Biology, 1996. **181**(2): p. 179-196.

97. Chittka, L., *Bee color vision is optimal for coding flower color, but flower colors are not optimal for being coded - Why?* Israel Journal of Plant Sciences, 1997. **45**: p. 115-127.

98. Menzel, R. and A.V.I. Shmida, *The ecology of flower colours and the natural colour vision of insect pollinators: The Israeli flora as a study case.* Biological Reviews - BIOL REV, 1993. **68**: p. 81-120.

99. Gumbert, A., J. Kunze, and L. Chittka, *Floral colour diversity in plant communities, bee colour space and a null model.* Proceedings of the Royal Society of London. Series B: Biological Sciences, 1999. **266**(1429): p. 1711-1716.

100. Garbers, C. and T. Wachtler, *Wavelength Discrimination in Drosophila Suggests a Role of Rhodopsin 1 in Color Vision.* PLoS ONE, 2016. **11**(6): p. e0155728.

101. Yatsenko, D., E.Y. Walker, and A. Tolias, *DataJoint: A Simpler Relational Data Model.* ArXiv, 2018. **abs/1807.11104**.

102. Sharkey, C.R., et al., *The spectral sensitivity of Drosophila photoreceptors.* Scientific Reports, 2020. **10**(1): p. 18242.

103. Yamashita, S. and H. Tateda, *Spectral sensitivities of jumping spider eyes.* Journal of comparative physiology, 1976. **105**(1): p. 29-41.

104. Chen, D.M. and T.H. Goldsmith, *Four spectral classes of cone in the retinas of birds.* Journal of Comparative Physiology A, 1986. **159**(4): p. 473-479.

105. Baylor, D.A., B.J. Nunn, and J.L. Schnapf, *Spectral sensitivity of cones of the monkey Macaca fascicularis.* The Journal of Physiology, 1987. **390**(1): p. 145-160.

106. Armington, J.C., *Spectral sensitivity of the turtle, Pseudemys.* Journal of Comparative and Physiological Psychology, 1954. **47**(1): p. 1-6.

107. Endeman, D., L.J. Klaassen, and M. Kamermans, *Action Spectra of Zebrafish Cone Photoreceptors.* PLOS ONE, 2013. **8**(7): p. e68540.

108. Palacios, A.G., et al., *Spectral sensitivity of cones in the goldfish, Carassius auratus.* Vision Research, 1998. **38**(14): p. 2135-2146.

109. Bennett, R.R. and P. Ruck, *Spectral sensitivities of dark- and light-adapted Notonecta compound eyes.* Journal of Insect Physiology, 1970. **16**(1): p. 83-88.

110. Yang, E.-C. and D. Osorio, *Spectral sensitivities of photoreceptors and lamina monopolar cells in the dragonfly, Hemicordulia tau.* Journal of Comparative Physiology A, 1991. **169**: p. 663-669.

111. Belusic, G., K. Sporar, and A. Meglič, *Extreme polarization sensitivity in the retina of the corn borer moth Ostrinia.* The Journal of Experimental Biology, 2017. **220**: p. jeb.153718.

112. Katz, B. and B. Minke, *Drosophila photoreceptors and signaling mechanisms.* Frontiers in Cellular Neuroscience, 2009. **3**(2).

113. Montell, C., *Visual transduction in Drosophila.* Annual review of cell and developmental biology, 1999. **15**(1): p. 231-268.

114. Colman, A.M., *A dictionary of psychology*. A dictionary of psychology. 2001, New York, NY, US: Oxford University Press. xv, 844-xv, 844.

115. Pagni, M., et al., *Interaction of "chromatic" and "achromatic" circuits in Drosophila color opponent processing.* Current Biology, 2021. **31**(8): p. 1687-1698.e4.

116. Li, Y., et al., *Neural mechanism of spatio-chromatic opponency in the Drosophila amacrine neurons.* Current Biology, 2021.

117. Vanleeuwen, M.T., et al., *The contribution of the outer retina to color constancy: a general model for color constancy synthesized from primate and fish data.* Vis Neurosci, 2007. **24**(3): p. 277-90.

118. Sabbah, S., et al., *Feedback from horizontal cells to cones mediates color induction and may facilitate color constancy in rainbow trout.* PLoS One, 2013. **8**(6): p. e66216.

119. Kamermans, M., D.A. Kraaij, and H. Spekreijse, *The cone/horizontal cell network: a possible site for color constancy.* Vis Neurosci, 1998. **15**(5): p. 787-97.

120. Neumeyer, C., *Chromatic adaptation in the honeybee: Successive color contrast and color constancy.* Journal of comparative physiology, 1981. **144**(4): p. 543-553.

121. Werner, A., R. Menzel, and C. Wehrhahn, *Color constancy in the honeybee.* The Journal of Neuroscience, 1988. **8**(1): p. 156.

122. Takemura, S.Y., et al., *Synaptic circuits and their variations within different columns in the visual system of Drosophila.* Proc Natl Acad Sci U S A, 2015. **112**(44): p. 13711-6.

123. Talay, M., et al., *Transsynaptic Mapping of Second-Order Taste Neurons in Flies by trans-Tango.* Neuron, 2017. **96**(4): p. 783-795.e4.

124. Panser, K., et al., *Automatic Segmentation of Drosophila Neural Compartments Using GAL4 Expression Data Reveals Novel Visual Pathways.* Current Biology, 2016. **26**(15): p. 1943-1954.

125. Timaeus, L., et al., *Parallel Visual Pathways with Topographic versus Nontopographic Organization Connect the Drosophila Eyes to the Central Brain.* iScience, 2020. **23**(10): p. 101590.

126. Hardcastle, B.J., et al., *A visual pathway for skylight polarization processing in Drosophila.* eLife, 2021. **10**: p. e63225.

127. El Jundi, B., et al., *Integration of polarization and chromatic cues in the insect sky compass.* Journal of Comparative Physiology A, 2014. **200**(6): p. 575-589.

128. Mota, T., et al., *Chromatic processing in the anterior optic tubercle of the honey bee brain.* J Neurosci, 2013. **33**(1): p. 4-16.

129. Pfeiffer, K. and U. Homberg, *Coding of azimuthal directions via time-compensated combination of celestial compass cues.* Curr Biol, 2007. **17**(11): p. 960-5.

130. Kinoshita, M., K. Pfeiffer, and U. Homberg, *Spectral properties of identified polarized-light sensitive interneurons in the brain of the desert locust Schistocerca gregaria.* J Exp Biol, 2007. **210**(Pt 8): p. 1350-61.

131. Wu, M., et al., *Visual projection neurons in the Drosophila lobula link feature detection to distinct behavioral programs.* Elife, 2016. **5**.

132. Stopfer, M., *Central processing in the mushroom bodies.* Curr Opin Insect Sci, 2014. **6**: p. 99-103.

133. Vogt, K., et al., *Direct neural pathways convey distinct visual information to mushroom bodies.* Elife, 2016. **5**.

134. Vogt, K., et al., *Shared mushroom body circuits underlie visual and olfactory memories in Drosophila.* Elife, 2014. **3**: p. e02395.

135. Little, C.M., et al., *Color preference of the spotted wing Drosophila, Drosophila suzukii.* Scientific Reports, 2019. **9**(1): p. 16051.

136. Longden, K. and M. Reiser, *Color vision for flight control in Drosophila.* Journal of Vision, 2017. **17**(10): p. 395-395.

137. Keene, A.C., et al., *Distinct Visual Pathways Mediate Drosophila Larval Light Avoidance and Circadian Clock Entrainment.* The Journal of Neuroscience, 2011. **31**(17): p. 6527.